Semidiurnal Internal Tide Energy Fluxes and their Variability in a Global Ocean Model and Moored Observations

Joseph K. Ansong,[1] Brian K. Arbic[1], Matthew H. Alford[2], Maarten C. Buijsman[3], Jay F. Shriver[4], Zhongxiang Zhao[5], James G. Richman[6], Harper L. Simmons[7], Patrick G. Timko[8], Alan J. Wallcraft[4], Luis Zamudio[6]

Corresponding author: Joseph K. Ansong, Department of Earth & Environmental Sciences, University of Michigan, Ann Arbor, Michigan, USA. (jkansong@umich.edu)

[1]Department of Earth & Environmental

Abstract. We examine the temporal means and variability of the semidiurnal internal tide energy fluxes in 1/25° global simulations of the HYbrid Coordinate Ocean Model (HYCOM) and in a global archive of 79 historical moorings. Low-frequency flows, a major cause of internal tide variability, have comparable kinetic energies at the mooring sites in model and observations. The computed root-mean-square (RMS) variability of the energy flux is large in both model and observations and correlates positively with the time-averaged flux magnitude. Outside of strong generation regions, the normalized RMS variability (the RMS variability divided by the mean) is nearly independent of the flux magnitudes in the model, and of order 23 % or more in both the model and observations. The spatially averaged flux magnitudes in observations and the simulation agree to within a factor of about 1.4 and 2.4 for vertical modes-1 and -2 respectively. The difference in energy flux computed from the full-depth model output versus model output subsampled at mooring instrument depths is small. The global historical archive is supplemented with six high-vertical resolution moorings from the Internal Waves Across the Pacific (IWAP) experiment. The model fluxes agree more closely with the high-resolution IWAP fluxes than with the historical mooring fluxes. The high variability in internal tide energy fluxes implies that internal tide fluxes computed from short observational records should be regarded as realizations of a highly variable field, not as "means" that are indicative of conditions at the measurement sites over all time.

Sciences, University of Michigan, Ann

1. Introduction

This paper is about internal tide energy fluxes, and their temporal variability, in global models and a global archive of historical observations. Internal tides are one of the most important sources of energy for mixing the deep ocean [*Munk and Wunsch*, 1998; *Wunsch and Ferrari*, 2004; *Egbert and Ray*, 2000, 2001]. The ocean tides are due to the differential gravitational pull of the Sun and Moon across the finite extent of the Earth. The ocean responds to these forces via oscillations in sea surface elevation along with corresponding horizontal tidal currents throughout the water column. Because the ocean is stratified, the flow of the barotropic tide over topographic features results in isopycnal displacements along with associated baroclinic currents. Such internal waves of tidal frequency are called internal tides. Internal tides propagate for thousands of kilometers across ocean basins [*Dushaw et al.*, 1995; *Ray and Mitchum*, 1996, 1997; *Mitchum and Chiswell*, 2000; *Zhao et al.*, 2010, 2016; *Ray and Zaron*, 2016].

Though recognized as important tools for studying internal tides, global internal tide models (e.g. *Arbic et al.* [2004]; *Simmons et al.* [2004]; *Hibiya et al.* [2006]; *Simmons* [2008]; *Arbic et al.* [2010]; *Simmons and Alford* [2012]; *Müller et al.* [2012]; *Müller* [2013]; *Müller et al.* [2014]; *Rocha et al.* [2016]) are computationally expensive and so are rarer than regional internal tide models. The HYbrid Coordinate Ocean Model (HYCOM) tidal simulations (e.g. *Arbic et al.* [2010, 2012]) are used for operational purposes by the United States Navy, and have been compared to field and remotely sensed measurements. *Shriver et al.* [2012] and *Ansong et al.* [2015] compared the barotropic and internal tide sea

Arbor, Michigan, USA.

surface elevation signals in HYCOM with those in altimeter-constrained products. *Timko et al.* [2012, 2013] compared the three-dimensional tidal kinetic energy field in HYCOM with kinetic energies computed from archived moored current meter records. *Müller et al.* [2015] compared the internal gravity wave continuum kinetic energy frequency spectra in HYCOM with spectra computed from moored current meters. *Buijsman et al.* [2016] computed the tidal energy fluxes and conducted a tidal energy balance analysis of a 1/12.5° HYCOM model. None of the previous comparisons of HYCOM internal tides with observations have focused on internal tide energy fluxes, the focus of our study here.

Much of what we know about internal tide energy fluxes, and their temporal variability, has been gleaned from studies with a regional focus, or from theoretical and idealized studies (e.g. *St. Laurent and Garrett* [2002]; *Ponte and Klein* [2015]). Direct simulation or estimation of the baroclinic tides and the associated energy fluxes has been done on regional scales (e.g. *Cummins and Oey* [1997]; *Merrifield et al.* [2001]; *Merrifield and Holloway* [2002]; *Rainville et al.* [2010]; *Carter et al.* [2012]; *Buijsman et al.* [2014]; *Zaron and Egbert* [2014]; *Zaron* [2015]; *Kerry et al.* [2014, 2016]; *Alford et al.* [2015]), for example around the Hawai'ian ridge, South China Sea and other regions. Several previous studies demonstrate the complex interference patterns of baroclinic energy fluxes and caution that multiple waves need to be considered when comparing pointwise observations with regional models (e.g. *Rainville et al.* [2010]; *Zhao et al.* [2010]). *Zaron and Egbert* [2014] forced their regional tidal model with time-varying subtidal background fields, taken from a different model, to study the refraction of the internal tide by large-scale time-varying

[2]Scripps Institution of Oceanography,

stratification. *Zaron and Egbert* [2014] could not find a quantitative agreement between the modeled and observed mean fluxes and attributed this, in part, to topographic errors and deficiencies in the background stratification. In contrast to the approach used by *Zaron and Egbert* [2014], in which the eddy field estimated from a separate model was then used in an internal tide model, our global model is simultaneously forced by the tides and atmospheric fields. Therefore, the scattering effects of mesoscale eddies on internal tides takes place via interactions within the same simulation. However, the $1/25^\circ$ horizontal resolutions of the simulations used here are not as high as the $1/30^\circ$ resolution used in *Zaron and Egbert* [2014].

To the best of our knowledge, the present study is the only one to compare internal tide energy fluxes in models and observations on a global scale (as opposed to comparisons done in specific regions). We note that *Simmons and Alford* [2012] compared the near-inertial wave (NIW) energy fluxes in a global model to NIW fluxes computed from moored and shipboard measurements of currents. The energy flux is a fundamental and important quantity in internal wave energetics because it identifies wave propagation, and because the divergence of the energy flux quantifies energy sources and sinks [*Nash et al.*, 2005]. Because the energy flux is a higher-order quantity it may be more difficult to model correctly than, for instance, sea surface elevations. It is therefore necessary to investigate how well state-of-the-art global high-resolution internal tide models can simulate internal tide energy fluxes. In addition, previously published global observational study on internal tide energy fluxes [*Alford and Zhao*, 2007] did not quantitatively investigate the temporal variability in the fluxes. This quantification of internal tide temporal variability is a

University of California, San Diego, USA.

major effort in this new study. The presence of atmospheric forcing in our high-resolution model ensures a vigorous mesoscale eddy field [*Hecht and Hasumi*, 2008], comparable to observations, and yields large variabilities in the internal tides (e.g. *Shriver et al.* [2014]). We will argue that, because of the large variabilities in both model and observations, the internal tide energy fluxes inferred from short (about a month-long) observational records should be viewed as realizations of a highly variable field. Similar points have been made in regional studies (e.g. *Kerry et al.* [2016]), but ours is, to the best of our knowledge, the first to make this point using models and datasets on a global scale.

A significant focus in our global model-data comparisons is the temporal variability of the tidal energy fluxes. *Shriver et al.* [2014] examine the non-stationarity of the internal tide sea surface height (SSH) signature in HYCOM (see also *Ray and Zaron* [2011], who studied internal tide SSH non-stationarity using along-track altimeter data). *Shriver et al.* [2014] show that, away from internal tide generation regions, the non-stationary internal tide can be comparable to or larger than the stationary internal tide. Here, in contrast to *Shriver et al.* [2014] and *Zaron and Egbert* [2014], we will discuss the temporal variability of band-passed semidiurnal internal tide energy fluxes, rather than using harmonic analysis to draw out separate tidal constituents. We do not use harmonically analyzed fields here because our goal is to compare the energy fluxes from our global model to those derived from historical moored observations. Our analysis procedure is as close as possible to the approach used in the observations by *Alford and Zhao* [2007], who used bandpassing as described further below.

---

[3]Department of Marine Science,

We compare the HYCOM baroclinic tidal energy fluxes with the vertical mode-1 and -2 fluxes computed from 79 historical moorings by *Alford and Zhao* [2007]; hereafter, AZ07. Historical moored records have a small number of instruments in the vertical direction. For

University of Southern Mississippi, 1020
Balch Blvd, Stennis Space Center, MS,
USA.

[4]Ocean Dynamics and Prediction Branch,
Code 7323, Naval Research Laboratory,
Stennis Space Center, MS, USA.

[5]Applied Physics Laboratory and School
of Oceanography, Seattle, Washington,
USA.

[6]Center for Ocean and Atmospheric
Prediction, Florida State University,
Tallahassee, FL, USA.

[7]International Arctic Research Center,
University of Alaska-Fairbanks, Fairbanks,
AK 99775, USA.

[8]Centre for Applied Marine Sciences,
Bangor University, Menai Bridge, Anglesey,
LL59 5AB, UK.

instance, only 10 of the 79 locations have 10 or more mooring instruments in the water column; most have 4 or 5. AZ07 estimate the errors involved in computing the fluxes from different vertical samplings of mooring instruments following procedures outlined in *Nash et al.* [2005]. For the worst configuration of a four instrument mooring with a large gap at the top of the water column, errors can approach 100 %. For more optimal distributions of mooring instruments, errors are $O(10 - 20\,\%)$. In five locations, AZ07 find that the vertical distribution of mooring instruments was only sufficient to resolve the first mode. Thus, we similarly exclude the mode-2 flux calculations from those five locations in our analysis. Motivated by the low vertical resolution in historical mooring records, we will separately compare fluxes (from one-year-long $1/25^\circ$ HYCOM output) to fluxes computed from 6 profiling moorings used in the Internal Waves Across the Pacific (IWAP) experiment [*Alford et al.*, 2007; *Zhao et al.*, 2010]. The profiling moorings have very high vertical resolution (2 meters) but are of short duration (about 2 months or less). We will also compare results from model output that is vertically subsampled, to mimic the sparse vertical coverage of historical moorings, with fluxes computed from full-water-column model output.

In section 2 we give a brief description of the HYCOM simulations and observational data. Section 3 presents the methods used to perform vertical modal decompositions of the model output, describes the energy flux calculations, defines the metric of variability, and introduces some statistical measures we will use in our model-data comparisons. The main results are presented in section 4 and we give the conclusions in section 5.

2. The HYCOM simulations and observations

The simulations used in this study are performed with HYCOM (*Bleck* [2002]; *Chassignet et al.* [2009]; *Halliwell* [2004]), which is in use by the United States Navy as an operational model [*Metzger et al.*, 2014]. The simulations are forced by the three largest semidiurnal tidal constituents (M_2, S_2, N_2) and the two largest diurnal tidal constituents (K_1, O_1). Concurrent with the astronomical tidal forcing, the HYCOM simulations are forced by atmospheric fields from the Navy Global Environmental Model (NAVGEM; *Hogan et al.* [2014]). The simulations employ tidal Self Attraction and Loading (SAL; *Hendershott* [1972]; *Ray* [1998]) fields calculated from the data-assimilative TPXO8-atlas [*Egbert and Erofeeva*, 2002] and use the parameterized topographic wave drag scheme of *Jayne and St Laurent* [2001]. Because global models are not able to resolve the breaking of internal waves, *Arbic et al.* [2004, 2010] argue that a parameterized wave drag acting on the bottom flow is needed in global internal tide models, to represent the generation and breaking of unresolved high vertical modes by flow over topography. Consistent with this, *Shriver et al.* [2012] and *Ansong et al.* [2015] showed that the barotropic and low-mode baroclinic tides from simulations forced by tides and atmospheric fields compare more closely to satellite altimeter observations when a parameterized internal wave drag is applied to the bottom flow. In contrast to our previous HYCOM tide simulations [*Arbic et al.*, 2010, 2012; *Richman et al.*, 2012; *Shriver et al.*, 2012, 2014; *Timko et al.*, 2012, 2013; *Stammer et al.*, 2014; *Buijsman et al.*, 2015, 2016; *Müller et al.*, 2015; *Ansong et al.*, 2015] which were run in purely forward (non-data-assimilative) mode, the simulations used here incorporate an Augmented State Ensemble Kalman filter (ASEnKF; *Ngodock et al.* [2016]) to reduce barotropic tidal SSH errors. The M_2 sea surface elevation error, computed over gridpoints equatorward of 66° and having seafloor depths exceeding

1000 m, of the HYCOM ASEnKF simulations used here is 2.6 cm [*Ngodock et al.*, 2016]. This error is substantially lower than errors reported in published studies of purely forward models (e.g., *Stammer et al.* [2014]), but is still higher than the errors in state-of-the-art assimilative barotropic tide models.

The simulations employed here have 41 hybrid vertical coordinate surfaces, with nominal horizontal resolutions of 1/12.5° and 1/25° at the equator. The 1/12.5° simulations were run from July 2011 through October 2012 and hourly time series output at model grid points nearest to the mooring locations was saved for 183 days from October 2011 to March 2012. The 1/25° simulation was run from November 2013 through December 2014 and hourly time series output at nearest neighbor mooring locations was saved for one year from January 2014 to December 2014. This paper focuses primarily on the 1/25° simulation because of the longer output record and higher horizontal resolution. The 1/12.5° simulation is used to demonstrate a few conceptual points.

Figure 1 shows the locations of the 79 historical moorings from which internal tide energy fluxes were derived from hourly time series data in AZ07. Most of the moorings are located in the North Atlantic ocean, and very few are in the Southern Hemisphere. The mooring records spanned more than 30 years. Only moorings with a record length greater than 180 days were used to compute the fluxes. Forty-five moorings have a record length of at least one year. Additional details of the mooring data and the computation of modal energy fluxes from them can be found in AZ07.

3. Methods

3.1. Vertical mode decomposition

To be consistent with AZ07, the HYCOM output is first bandpassed for the semidiurnal components with a fourth-order Butterworth filter having zero-phase response centered at the M_2 frequency between $1.55 - 2.42$ cycles/day. As in the AZ07 treatment of the historical mooring data, we decompose the HYCOM bandpassed output into vertical modes. The vertical structure of internal tides in HYCOM can be decomposed into a linear combination of dynamical modes [*Wunsch*, 1975] such that

$$\boldsymbol{u}(z,t) = \sum_{m=0}^{M} \boldsymbol{u}_m(t)\Phi_m(z), \qquad \eta(z,t) = \sum_{m=1}^{M} \eta_m(t)\chi_m(z) \tag{1}$$

where $\boldsymbol{u} = (u, v)$ is the horizontal velocity and η is the isopycnal displacement, m is an index of vertical mode number, z is the vertical coordinate, t is time, M is the total number of vertical modes employed, and $\Phi_m(z)$ and $\chi_m(z)$ are the vertical structure functions of the mth baroclinic mode of velocity and displacement fields respectively. Note that the velocity decomposition also includes the barotropic mode, $m = 0$. The linear dynamical modes are calculated from the buoyancy frequency, $N(z)$, and satisfy the following equations [*Wunsch*, 1975; *Gill*, 1982; *Wunsch and Stammer*, 1997]

$$\frac{\mathrm{d}}{\mathrm{d}z}\left(\frac{\omega^2 - f^2}{N^2(z) - \omega^2}\frac{\mathrm{d}\Phi_m(z)}{\mathrm{d}z}\right) + \lambda_m^2\Phi_m(z) = 0 \tag{2}$$

with boundary conditions

$$\frac{\mathrm{d}\Phi_m(z)}{\mathrm{d}z} = 0, \quad z = 0, -H \tag{3}$$

and

$$\frac{\mathrm{d}^2\chi_m(z)}{\mathrm{d}z^2} + \left(\frac{N^2(z) - \omega^2}{\omega^2 - f^2}\right)\lambda_m^2\chi_m(z) = 0 \tag{4}$$

with boundary conditions

$$\chi_m(z) = 0, \quad z = 0, -H, \tag{5}$$

where H is the water depth, f is the Coriolis frequency, ω is the M_2 internal tide frequency and λ_m^2 represents the eigenvalue of the mth vertical mode. The vertical eigenfunctions $\Phi_m(z)$ and $\chi_m(z)$ are orthonormal such that [*Flierl*, 1978; *Gill*, 1982]

$$\frac{1}{\mathcal{H}} \int_{z=-H}^{0} \Phi_n(z)\Phi_m(z)\mathrm{d}z = \delta_{mn}, \tag{6}$$

$$\frac{1}{\mathcal{G}} \int_{z=-H}^{0} W(z)\chi_n(z)\chi_m(z)\mathrm{d}z = \delta_{mn}, \tag{7}$$

where δ_{mn} is the Kronecker delta, $W(z) = \left(N^2(z) - \omega^2\right)/(\omega^2 - f^2)$, $\mathcal{H} = \int_{z=-H}^{0} \Phi_n(z)^2\mathrm{d}z$, and $\mathcal{G} = \int_{z=-H}^{0} W(z)\chi_n(z)^2\mathrm{d}z$. Equations (2)-(5) may be solved for the eigenfunctions and eigenvalues using either a matrix approach or the so-called shooting method (*Emery and Thomson* [1997], chapter 4). Here, we solve the equations using a shooting method code (Glenn Flierl, Personal Communications 1995). The shooting method code yields results that are orthonormal to high precision ($\delta_{n\neq m} \sim 10^{-7}$) for $\Phi_m(z)$ and to a moderate precision ($\delta_{n\neq m} \sim 10^{-3}$) for $\chi_m(z)$. After computing the eigenfunctions, we then obtain the time-dependent modal components $\boldsymbol{u}_m(t)$ and $\eta_m(t)$ from equation (1) via a least square regression method for the barotropic mode and the first two baroclinic modes.

3.2. Energy and energy flux calculations

For each vertical mode, the depth-integrated horizontal kinetic energy, HKE, and the available potential energy, APE, are computed by

$$\mathrm{HKE} = \frac{1}{2}\bar{\rho} \int_{-H}^{0} < |\mathbf{u}(z',t)|^2 > \mathrm{d}z', \tag{8}$$

$$\mathrm{APE} = \frac{1}{2}\bar{\rho} \int_{-H}^{0} < N^2(z')\eta^2(z',t) > \mathrm{d}z', \tag{9}$$

where $<>$ denotes a time average, and $\bar{\rho}$ is water density.

To calculate the model energy flux for each vertical mode, we first interpolate the HYCOM output to equally-spaced $z-$levels and then compute the depth-integrated baroclinic energy flux, $\mathbf{F}$, following the method presented in previous studies [*Kunze et al.*, 2002; *Nash et al.*, 2005; *Alford and Zhao*, 2007; *Zhao et al.*, 2010], viz.

$$\mathbf{F} = \int_{-H}^{0} < \mathbf{u}(z')p'(z') > \mathrm{d}z', \tag{10}$$

where p' is the baroclinic pressure anomaly. The baroclinic pressure anomaly is calculated for each vertical mode m as

$$p'_m(z) = \bar{\rho} \int_{-z}^{0} N^2(z')\eta_m(z')\mathrm{d}z' - \bar{p}_m, \tag{11}$$

where $\bar{p}_m$ is the mean defined as

$$\bar{p}_m = \bar{\rho} \int_{-H}^{0} N^2(z')\eta_m(z')\mathrm{d}z'. \tag{12}$$

A second approach for computing energy fluxes from layered model variables is given in appendix A, along with a comparison of the resulting fluxes with those used in our primary method given above. Because historical moored instrument records generally lack salinity measurements, AZ07 computed energy fluxes using temperature anomalies as a proxy for density anomalies. The AZ07 vertical displacements were computed via the relation $\eta(z_i, t) = T(z_i, t)/T_z(z_i)$, where $T(z_i, t)$ is the bandpassed temperature measured at depth z_i and time t, and $T_z(z_i)$ is the vertical temperature gradient. To avoid unrealistic displacements, instruments where $T_z < 3 \times 10^{-5}\,^{\circ}\mathrm{Cm}^{-1}$, or where T increases toward the seafloor, were removed from their calculations. The AZ07 approach would be problematic in HYCOM, because HYCOM generally has very thick isopycnal layers in the deep ocean, resulting in negligible abyssal temperature variability in HYCOM fields that employ in-

terpolation to equally-spaced depth levels. Therefore, we compute the HYCOM vertical displacements directly from the model layer thicknesses instead of the temperature fields.

3.3. Energy flux variability calculations

To compute the temporal variability in both the HYCOM and observed baroclinic energy fluxes we divide our time series into 50 % overlapping 30−day windows. The variance in the fluxes is then computed by adapting the approach used in *Shriver et al.* [2014] for a scalar variable to a vector quantity. We define

$$\sigma^2 = \frac{1}{n}\sum_{j=1}^{n} |F_j e^{i\phi_j} - \bar{F}e^{i\bar{\phi}}|^2, \tag{13}$$

where n is the number of overlapping windows, F is the magnitude and ϕ is the direction (angle; measured from due East) of the baroclinic energy fluxes, and the overbar denotes an average computed over all n windows. Explicitly,

$$F_j e^{i\phi_j} = \frac{1}{s}\sum_{k=1}^{s} F_k e^{i\phi_k} \quad \text{and} \quad \bar{F}e^{i\bar{\phi}} = \frac{1}{n}\sum_{j=1}^{n} F_j e^{i\phi_j}, \tag{14}$$

where s is the length of data in a window ($30 \times 24 = 720$ hours). The square root of (13) is referred to as the "total variability". To investigate the individual contributions to the variability by the magnitude and the direction of fluxes, equation (13) is rewritten as [*Shriver et al.*, 2014]

$$\sigma^2 = \left(\frac{1}{n}\sum_{j=1}^{n}\left(F_j - \bar{F}\right)^2\right) + \left(\frac{1}{n}\sum_{j=1}^{n}\left[2F_j\bar{F}(1-\cos(\phi_j - \bar{\phi}))\right]\right). \tag{15}$$

The square root of the first term on the right hand side, referred to as the "magnitude-only" variability, captures the contribution to the variability due solely to the time-varying magnitudes of the energy fluxes. The square root of the second term, referred to as the "magnitude-weighted direction" variability, is due solely to the time-variability in the

directions, weighted by the magnitude of the fluxes. The variability due solely to the directions may be estimated by replacing F_j with $\bar{F}$ in the second term and is denoted as the "direction-only" variability. As in *Shriver et al.* [2014], the normalized RMS variability (NRMS), the RMS variability divided by the mean ($\bar{F}$), is used as a normalized metric for variability.

3.4. Regression analysis

In our HYCOM-mooring comparison we use statistical measures to quantify the spatial variability in the baroclinic energy fluxes. We especially rely on regression and correlation analysis (see *Emery and Thomson* [1997], chapter 3). The linear regression between modeled and observed magnitudes of energy fluxes, $F = |\mathbf{F}|$, is given by $F_{mod} = A \cdot F_{obs}$, where the subscripts *mod* and *obs* refer to model and observations respectively. A is the regression coefficient (the slope of the regression line) given by

$$A = \frac{\sum_{i=1}^{\mathcal{N}} F_{obs} F_{mod}}{\sum_{i=1}^{\mathcal{N}} F_{obs}^2}, \tag{16}$$

where $\mathcal{N}$ is the total number of locations. A minimizes the square of the difference between the modeled and observed energy fluxes. The correlation coefficient R determines how well the observed and modeled energy fluxes co-vary in space. It is related to the regression coefficient by

$$R = A \cdot \frac{\sqrt{\sum_{i=1}^{\mathcal{N}} (F_{obs} - \bar{F}_{obs})^2}}{\sqrt{\sum_{i=1}^{\mathcal{N}} (F_{mod} - \bar{F}_{mod})^2}}, \tag{17}$$

where variables with overbars denote spatial mean values. The coefficient of determination, R^2, represents the percentage of variance explained by the linear relationship between F_{mod} and F_{obs}. The gross magnitude of energy fluxes in the model compared to

observations may also be assessed with the ratio of their global mean values:

$$\gamma = \frac{\sum_i^{\mathcal{N}} F_{mod}}{\sum_i^{\mathcal{N}} F_{obs}}. \tag{18}$$

Finally, the angle between the time-averaged modeled and observed flux vector at each location, ϕ_b, is also used to assess the skill of HYCOM with regard to the direction of energy flux. The fraction of locations with $\phi_b \leq 60°$ is computed and is denoted by γ_{dir}.

4. Results

We present the energy fluxes obtained after performing vertical mode decompositions on the model output. The model energy flux is computed in two ways: (1) on the full-depth model data (referred to as "full-column") and (2) on model output subsampled at the mooring instrument depths (referred to as "subsampled"). The subsampling is done to determine the impact of the sparse vertical sampling in the historical records on the tidal energy flux estimates made from them. Two Southern Ocean locations at which the mean magnitude of energy flux in HYCOM is less than 10^{-4} kW/m have been removed from the analysis.

In a separate analysis to be presented in section 4.4, we compare the semidiurnal energy fluxes from 1/25° HYCOM to those derived from the IWAP experiment [*Alford et al.*, 2007; *Zhao et al.*, 2010]. In this case the HYCOM output is bandpassed using a fourth-order Butterworth filter with zero-phase response centered at the M_2 frequency between $1.73 - 2.13$ cycles/day, consistent with *Zhao et al.* [2010]. As in *Zhao et al.* [2010], the HYCOM output is solved for the first 5 baroclinic modes before computing the energy fluxes from the first two modes. Note that "fluxes" in the text means time-averaged fluxes unless stated otherwise.

4.1. Tidal fluxes, conversion rates and modal energy density

Before comparing fluxes in HYCOM and observations at the mooring locations, we present global maps of baroclinic energy fluxes and barotropic to baroclinic conversion rates from 1/12.5° HYCOM. Due to the large size of three-dimensional hourly model output datasets ($\sim$ 12 TB per model month), the global maps were made from just one month of 1/12.5° HYCOM output. The global maps, computed from the total baroclinic signals (i.e., without performing a vertical mode decomposition), demonstrate a rich and complex spatial variability. Figure 2*a*, the map of magnitudes of vertically-integrated baroclinic energy fluxes, reveals the beam-like structures of internal tides (e.g. *Simmons et al.* [2004]). As in previous studies [*Egbert and Ray*, 2003; *Simmons et al.*, 2004; *Niwa and Hibiya*, 2011; *Buijsman et al.*, 2016], the map of conversion rates (Figure 2*b*) reveals concentrated activity at hotspots such as mid-ocean ridges and shelf slopes. In particular we find high conversion rates in the Western Pacific, the Mid-Pacific ocean around Hawaii and the Tuamotu archipelago, the Drake Passage and Scotia Sea, along the Mid-Atlantic Ridge, and around Madagascar.

We next calculate the amount of baroclinic energy in the first two vertical modes and the fraction of baroclinic energy in mode-2. Figure 3 shows that the mode-1 waves are more energetic than mode-2 waves in most locations. On average, about 64 % of the energy resides in mode-1 with about 36 % in mode-2. We note here that the ratio of mode-1 to mode-2 energy flux (F_1/F_2) is generally much larger than the corresponding ratio in energy (E_1/E_2) because the mode-1 phase speed (c_1) is greater than that of mode-2 (c_2). The ratio c_1/c_2 at the mooring locations range from $1.2 - 2.4$ with a mean of about 2.0 over all locations.

4.2. Variability of energy flux

The temporal variability of the internal tides is primarily due to the presence of mesoscale eddies (e.g. *Zaron and Egbert* [2014]; *Ponte and Klein* [2015]). To investigate the energy levels in the modeled and observed mesoscale eddy fields, we compute the RMS of low-frequency eddy kinetic energy (EKE) using 2-day low-pass horizontal velocity time series at 51 mooring locations (Figure 4) at which unfiltered velocity fields from our historical archives are easily available. The spatially averaged RMS EKE in 1/12.5° HYCOM (HYCOM12) agrees to within a factor of about 2.4 of the average in the observations whereas 1/25° HYCOM (HYCOM25) agrees to within a factor of about 1.6. In both HYCOM12 and HYCOM25, the EKE is generally higher than in the observations (especially in HYCOM12) at these mooring locations. This is likely due to the small sample size used in the calculations here. *Thoppil et al.* [2011] find that the EKE in a HYCOM12 simulation is deficient compared to the EKE in a global drifter database, and by increasing the resolution to 1/25°, the EKE increased to values consistent with observations. In general we see that our HYCOM25 simulation is performing reasonably well with regards to the energy levels in the low-frequency field. Because the mesoscale eddies can de-cohere the internal tides, the scatter in Figure 4*b* can affect our model-data comparison of energy fluxes as discussed further in the paper. The rest of this paper uses results from our 1/25° HYCOM simulations.

Figure 5 displays an example time series of energy fluxes at a location north of Hawai'i (latitude 40.6° North, longitude 197.0° East). Both HYCOM and observational output are divided into 50 % overlapping 30−day windows and plotted with the envelopes (standard deviations) of the magnitude-only (Figure 5*a*) and direction-only (Figure 5*b*) variabilities

(see equation 15 and associated discussion). There is a large temporal variability in both observed and HYCOM fluxes. Figure 6 displays a location, at latitude 35.55° North and longitude 142.66° East, where the mean magnitude of the fluxes in HYCOM and observations match more closely but where there is still large variability about the mean. Below, we attempt to quantify these variabilities before doing a detailed comparison of model and observations.

The RMS total, magnitude-only, and magnitude-weighted direction variabilities in the mode-1 fluxes, computed using equations (13) and (15) from 50 % overlapping 30-day windows in 1/25° HYCOM and observations, are shown for all locations in Figure 7(a, b). The locations have been sorted by flux magnitude (for each dataset) in descending order, before plotting. The direction-only variability has similar values to the magnitude-weighted direction variability and is not plotted for the sake of clarity (see Table 1, which also gives mode-2 values). Figure 7(a, b) shows that in both 1/25° HYCOM and the observations the RMS variability generally decreases with decreasing mean magnitude of the fluxes. At many locations, especially in the observations, the total RMS variability is greater than the mean magnitude of the flux. The globally-averaged flux magnitude and the total RMS variability in HYCOM are 0.35 kW/m and 0.25 kW/m respectively, and the corresponding values for the observations are 0.44 kW/m and 0.5 kW/m (Table 1). Thus, the global mean RMS variability in the observations is higher than in HYCOM by a factor of about 2. In both HYCOM and observations, the contribution to the total RMS variability from the magnitude-only variability and magnitude-weighted direction variability are almost equal with the magnitude-only variability being a slightly larger contributor.

Following *Shriver et al.* [2014], we compute the normalized RMS variability (NRMS) as discussed in section 3. Figure 7*c* shows that the total NRMS in HYCOM remains nearly independent of location. However, in the observations (Figure 7*d*), locations with smaller fluxes tend to have larger NRMS. A likely reason for this discrepancy is that almost all the HYCOM locations analyzed in this study are outside of strong generation regions as discussed further below. The global mean values of NRMS (Table 1) imply that locations with relatively strong energy fluxes in HYCOM can be as equally variable as regions with weaker fluxes. This appears inconsistent with the HYCOM-based results of *Shriver et al.* [2014] who found that strong generation regions tend to be less variable (as measured by NRMS values) than other regions. The apparent inconsistency is likely due to the fact that the highly energetic regions captured in the global HYCOM-based analysis of *Shriver et al.* [2014] are missing in the present calculations due to the paucity of locations used. The minimum NRMS in mode-1 over all locations in HYCOM is about 23 % while that of the observations is about 58 %. Table 1 also shows that the mode-1 RMS and NRMS variabilities from the subsampled results are always larger than the full-column results, and always lie closer to the observed values. This implies that some of the disagreements between HYCOM and observation are due to the sparse vertical distribution of mooring instruments.

Figure 8 is the counterpart of Figure 7 but for mode-2, and shows that the mode-2 fluxes are generally weaker in both HYCOM and the observations. The overall decrease in RMS variability with decreasing strength of flux is similar to what we find in the mode-1 case. We see that in almost all locations, the total RMS variability is greater than the mean magnitude of energy flux. As in the mode-1 fluxes, the magnitude-only variability is a

slightly more important contributor to the total RMS variability. We find here that the NRMS in HYCOM and observations (Figure $8c-d$) show that variability appears to be roughly independent of the strength of the flux, especially in HYCOM.

Table 1 also indicates that the mode-2 waves are more variable than the mode-1 waves. The normalized RMS variability in both HYCOM and the observations is large. However, the globally-averaged NRMS values in the observations is consistently larger than in HYCOM. As in the mode-1 case, the subsampled mode-2 RMS variabilties are always larger and closer to the observed values. However, this is not always the case for the subsampled mode-2 NRMS values.

4.3. Comparison of mean flux magnitudes and direction

The results discussed above demonstrate that there are large temporal variabilities in the energy fluxes in both 1/25° HYCOM and the observations. One of the main sources of the large variabilities and complex spatial patterns of the internal tides is the presence of a vigorous mesoscale eddy field in the ocean. We thus expect some discrepancies between the modeled and observed energy fluxes. We next present the results of various statistical measures to roughly quantify the spatial correlation between the mean values of the fluxes in the model and in the observations. For the analysis in this section, the data is not divided into windows. Averages are computed using equal lengths of time series in both datasets. We note that in the observations each chunk of data will occur over different months of the year depending on location, whereas in the model the same months are always used. Thus, the model-data comparison in this section is unfortunately biased by seasonal sampling as described above. AZ07 find that, for the semidiurnal band, the energy flux does not display a strong dependence on season at the mooring locations,

consistent with the quasi-constant forcing of the tides. For the sake of conciseness, we do not repeat calculations of seasonal dependence here.

Figures 9 (left panels) and 10a compare, in scatterplots and in global maps respectively, the average mode-1 energy fluxes from the nearest neighbor grid location in 1/25° HYCOM to the semidiurnal mode-1 fluxes computed from moored observations. We see considerable scatter in the magnitude of the flux (Figure 9a). This is not so surprising considering the large temporal and complex spatial variability in both the model and observations. The regression and correlation coefficients A and R, and the γ values, are shown in Table 2, for both full-column and subsampled cases. The A, R, and γ values range from $0.68 - 0.96$, demonstrating that the model is doing reasonably well in predicting the spatial patterns of mode-1 fluxes. The coefficient of determination, $R^2 = 0.77$, indicates that about 77% of the variance can be explained by the linear relationship between the modeled and observed mode-1 flux magnitudes. A scatterplot of the mode-1 full-column versus subsampled HYCOM results is given in Figure 9c, showing minor differences between them. Figure 9e plots the angle between the HYCOM and observed energy fluxes, as well as the magnitude of the HYCOM fluxes, at each location. The locations have been sorted by HYCOM flux magnitudes in descending order. In the case of the mode-1 waves, the disagreement between the HYCOM and observed flux directions appears to be largest at locations with smaller energy fluxes; likely due to the fact that the direction of a vector becomes meaningless when the magnitude becomes very small. The fraction of locations where the angle between the HYCOM and observed fluxes is less than 60° is about 70 % (Figure 9e and Table 2). At 3 mooring locations inside the regions marked as hotspots in HYCOM, the mode-1 fluxes agree much more closely to

the observations (Table 3). We see that, apart from one location (28.08°N, 207.92°E) in which the mean flux magnitude differ greatly, the maximum difference in angle between the mode-1 fluxes in HYCOM and observations is about 15°. There are no apparent differences between the full-column versus the subsampled results at the 3 hotspot locations (Table 3).

Figures 9 (right panels) and 10*b* display similar results for the mode-2 fluxes. The statistical measures for the mode-2 fluxes are also given in Table 2. As expected from Figure 3, the mode-2 flux magnitudes are almost always smaller than the mode-1 flux magnitudes, in both HYCOM and the observations. There is greater scatter in the mode-2 case than in the mode-1 case resulting in lower values of the correlation coefficient. The globally averaged magnitude of the modeled mode-2 flux agrees with the observations to within a factor of about 2.4. Similar to the mode-1 case, there is some difference between the full-column versus subsampled results though we find a wider spread about the one-to-one line in this case (Figure 9*d*).

The agreement with the observed direction of propagation is poorer in the mode-2 case. The discrepancy with the direction of propagation for mode-2 is large even at the 3 hotspot locations (see Table 3). Again, the poorer agreement in flux direction in the mode-2 case may be due to the large variabilities in both model and observations, arising from the action of mesoscale eddies.

4.4. Comparison of 1/25° HYCOM to IWAP data

Figure 11*a* indicates that the mode-1 energy fluxes from 1/25° HYCOM compare well with fluxes derived from 6 profiling moorings from the IWAP experiment. There is a close correspondence in the magnitude of the fluxes and, apart from location MP3 where the

angle between the mode-1 fluxes from the two datasets is about 50°, the flux directions agree to within 30° or less (Figure 11*c*, Table 4). The mode-2 fluxes compare reasonably well but not as well as mode-1 (Table 4). Some of the largest disagreements in the mode-2 case occur at locations MP4, where the flux magnitudes differ, and MP5, where the flux directions differ greatly. As described in *Zhao et al.* [2010], locations MP1, MP2, MP3 and MP6 sampled their full range between 40 and 50 days, while MP4 and MP5 have spatial or temporal data gaps due to instrument failure. Thus, the data gaps in MP4 and MP5 affect our model-data comparison. Overall, HYCOM is performing reasonably well against the IWAP data considering the large interference from multiple waves in this region as emphasized by *Zhao et al.* [2010]. In contrast to a single propagating wave with constant energy flux and a constant ratio of horizontal kinetic to horizontal potential energy (HKE/HPE), the non-monotonicity of energy flux from MP1 to MP6 (Figure 11) as well as non-monotonicity of HKE/HPE (not shown) is indicative of wave interference (see also *Zhao et al.* [2010], where several other factors pointing to interference are described).

5. Summary and conclusions

Internal tide energy flux is a fundamental and important quantity in internal wave energetics because it identifies wave propagation, and because the divergence of the energy flux quantifies energy sources and sinks [*Nash et al.*, 2005]. It is important to compare the internal tide energy fluxes in global high resolution models used for operational and predictive purposes, such as HYCOM, to diverse observational data sets. Previous HYCOM versus observational internal tide and wave comparisons have focused on sea surface elevations, currents, and kinetic energy. However, attaining reasonably accurate internal tide

elevations in a global model does not guarantee that the model will have accurate energy fluxes. This is because the energy flux is a higher-order quantity involving the product of velocity and pressure, which may therefore be more difficult to model. In this paper, for the first time, we compare the internal tide energy fluxes from a global simulation (of 1/25° HYCOM) to a global observational dataset. In addition, we compute the variabilities in the energy fluxes in both model and observations, showing large variabilities in both data sets. The computation of internal tide flux variabilities in a global-scale observational dataset is another new feature of this work. The presence of a vigorous mesoscale eddy field in the model, comparable in strength to observations (as depicted in Figure 4*b*), is an important source of large variabilities in the internal tide energy fluxes. We argue that, because of the large variabilities in both model and observations, the internal tide energy fluxes inferred from short (about a month-long) observational records should be viewed as realizations of a highly variable field, rather than indicators of tidal energy fluxes over all time. A similar point has been made in *Kerry et al.* [2016] using regional models.

We compared the vertical mode-1 and -2 baroclinic tidal energy fluxes from global 1/25° HYCOM simulations to fluxes derived from a global archive of historical mooring records [*Alford and Zhao*, 2007] and to fluxes derived from six profiling moorings deployed in the Internal Waves Across the Pacific (IWAP) experiment [*Alford et al.*, 2007; *Zhao et al.*, 2010]. Computations are done from the full-depth model output as well as from model output subsampled at the historical mooring depths. The subsampling is done to determine the effect of sparse vertical sampling on the energy flux estimates. We also computed the RMS variability in both the 1/25° HYCOM and observational energy fluxes using 50 % overlapping 30−day data windows. In addition, various statistical measures

were computed to help quantity the spatial correlation of the two data sets. In the case of the mode-1 fluxes, we find that

1) the spatially-averaged total RMS variability about the mean is larger in the observations than in HYCOM by a factor of about 2. The normalized RMS variability (NRMS), computed as in *Shriver et al.* [2014], is roughly independent of location in HYCOM, but is less so in the observations. This implies that, outside of the regions marked as hotspots in HYCOM [*Shriver et al.*, 2014], variability appears roughly independent of the magnitude of the energy flux at the mooring locations. The spatial mean values of NRMS in HYCOM and the observations is around 1.31 and 1.74 respectively.

2) though there is considerable scatter in the data, HYCOM displays reasonably high skill in correlating the geographical patterns of the flux magnitude. The correlation coefficient R is about 0.88. Spatial averages of fluxes computed from HYCOM and the observational time series agree to within a factor of about 1.4 (Table 2).

3) computing fluxes from model output vertically subsampled at the mooring depths partly explains the discrepancy between modeled and observed fluxes. For all locations, the statistical measures employed here show that the vertically subsampled results agree only slightly better with the observations than the full-column results.

4) the number of nearest-neighbor locations where the angle between the observed and modeled flux vectors lies within 60° is about 70 %. The relatively poor agreement between modeled and observed flux directions is likely due to the complex and strong spatial and temporal variability in both model and observations.

In the case of the mode-2 fluxes, we find that

1) the total RMS variability is greater than the mean magnitude flux in almost all locations in both HYCOM and the observations. The mode-2 fluxes show higher globally averaged NRMS values than the mode-1 fluxes and are also roughly independent of location, especially in HYCOM.

2) the spatially averaged 1/25° HYCOM flux magnitudes agree to within a factor of about 2.4 of the observations. The correlation is poorer in the mode-2 case than the mode-1 case, for both the magnitude and the direction of energy flux. We attribute this disagreement, in part, to the fact that the mode-2 fluxes are weaker and are more likely to be contaminated and/or modulated by other motions (see also *Zaron and Egbert* [2014]).

The mode-1 energy fluxes derived from six profiling moorings (with very high vertical resolution) deployed in the IWAP experiment agree quite well with 1/25° HYCOM (Figure 11*a*). Apart from one location where the angle between the mode-1 fluxes in the two datasets is about 50°, the remaining locations have directions that agree to within 30° or less. Furthermore, the mean flux magnitudes correlate reasonably well. The mode-2 fluxes in HYCOM and IWAP agree less well than the mode-1 fluxes, likely caused by some of the aforementioned factors.

Appendix A: Another approach to computing energy flux

The energy flux may also be computed directly from the native isopycnal model variables (see *Simmons et al.* [2004]). This second approach is convenient because there is no need to interpolate the model output to z-levels. However there are very few established methods for computing the vertical normal modes directly from layered model output (e.g. see *Lighthill* [1969]; *Simmons* [2008]). The observed fluxes were computed using the first approach (AZ07; section 3.2) so that we expect a more "apples-to-apples" comparison

using this method. Figure 12 demonstrates that there are minor differences in the model fluxes computed from our 1/12.5° simulation using the two different methods. There is a reasonably good agreement in the magnitude of the fluxes (Figure 12*a*). The angle between the fluxes using the two methods is less than 30° in about 96 % of the locations (Figure 12*b*, *c*). Figure 12*c*, which presents the locations in decreasing order of kinetic energy density, demonstrates that the differences in the angle between the fluxes are not directly related to energy levels.

Acknowledgments. Data sufficient to re-generate the figures, tables, and other results in this paper is stored on University of Michigan computers, and will be made freely available to members of the scientific community upon request. To obtain the data please contact the corresponding author (jkansong@umich.edu) or the second author (arbic@umich.edu). The raw output files for the model runs analyzed in this paper are archived at the Navy DSRC at the Stennis Space Center. The files stored there can be accessed after obtaining an account at the facility. The corresponding author can be contacted for information to access the archived data once an account has been established.

We thank two anonymous reviewers for very helpful comments leading to improvements in the manuscript. JKA, BKA, and PGT gratefully acknowledge support from National Science Foundation (NSF) grant OCE-0968783 and Office of Naval Research grants N00014-11-1-0487 and N00014-15-1-2288. HLS gratefully acknowledge support from NSF grant OCE-0968838. HLS, MHA and ZZ were supported by the project "Next-generation Global Altimetric Maps of Internal Tide Energy Flux and Dissipation" under NSF grant OCE-1130099. HLS and MHA were also supported by the project "Near-inertial wave studies using historical mooring records and a high-resolution general circulation model"

under Office of Naval Research (ONR) grant N00014-09-1-0399. MCB, JFS, JGR, AJW, and LZ were supported by the projects "Eddy resolving global ocean prediction including tides" and"Ageostrophic vorticity dynamics" sponsored by the ONR under program element 0602435N, and by N00014-11-1-2288. This work was supported in part by a grant of computer time from the Department of Defense (DoD) High Performance Computing Modernization Program at the Navy DoD Supercomputing Resource Center. This is NRL contribution NRL/JA/7320-2016-3156.

The work of JKA, BKA, MHA, and HLS on this project represents a contribution to the Climate Process Team (CPT) project "Collaborative Research: Representing Internal-Wave Driven Mixing in Global Ocean Models" which focuses on improving estimates of mixing due to internal waves in the ocean. The project is funded by the National Science Foundation and is led by Jennifer MacKinnon of the Scripps Institution of Oceanography.

References

Alford, M. H., and Z. Zhao (2007), Global patterns of low-mode internal-wave propagation. Part I: Energy and Energy flux, *Journal of Physical Oceanography*, *37*, 1829–1848.

Alford, M. H., J. MacKinnon, Z. Zhao, R. Pinkel, J. Klymak, and T. Peacock (2007), Internal waves across the Pacific, *Geophysical Research Letters*, *34, L24601*, 1–6, doi: 10.1029/2007GL031566.

Alford, M. H., T. Peacock, J. A. MacKinnon, J. D. Nash, M. C. Buijsman, L. R. Centuroni, C. M. H. Chao, S. Y., D. M. Farmer, O. B. Fringer, K. H. Fu, P. C. Gallacher, H. C. Graber, K. R. Helfrich, S. M. Jachec, C. R. Jackson, J. M. Klymak, D. Ko, S. Jan, T. M. S. Johnston, S. Legg, I. H. Lee, R. C. Lien, M. J. Mercier, J. N. Moum,

R. Musgrave, J. H. Park, A. I. Pickering, R. Pinkel, L. Rainville, S. R. Ramp, D. L. Rudnick, S. Sarkar, A. Scotti, H. L. Simmons, L. C. St Laurent, S. K. Venayagamoorthy, Y. Hwang, J. Wang, Y. J. Yang, T. Paluszkiewicz, and T. Y. Tang (2015), The formation and fate of internal waves in the South China Sea, *Nature*, *521*, 65–U381, doi:10.1038/nature14399.

Ansong, J. K., B. K. Arbic, M. C. Buijsman, J. G. Richman, J. F. Shriver, and A. J. Wallcraft (2015), Indirect evidence for substantial damping of low-mode internal tides in the open ocean, *Journal of Geophysical Research Oceans*, *120*, 6057–6071, doi: 10.1002/2015JC010998.

Arbic, B. K., S. T. Garner, R. W. Hallberg, and H. L. Simmons (2004), The accuracy of surface elevations in forward global barotropic and baroclinic tide models, *Deep-Sea Research II*, *51*, 3069–3101.

Arbic, B. K., A. J. Wallcraft, and E. J. Metzger (2010), Concurrent simulation of the eddying general circulation and tides in a global ocean model, *Ocean Modelling*, *32*, 175–187.

Arbic, B. K., J. G. Richman, J. F. Shriver, P. G. Timko, E. J. Metzger, and A. J. Wallcraft (2012), Global modeling of internal tides within an eddying ocean general circulation model, *Oceanography*, *25 (2)*, 20–29.

Bleck, R. (2002), An oceanic general circulation model framed in hybrid isopycnic-Cartesian coordinates, *Ocean Modelling*, *37*, 55–88.

Buijsman, M. C., J. Klymak, S. Legg, M. H. Alford, D. Farmer, J. A. MacKinnon, J. D. Nash, J.-H. Park, A. Pickering, and H. Simmons (2014), Three-dimensional double-ridge internal tide resonance in Luzon Strait, *Journal of Physical Oceanography*, *44*,

850–1356, doi:10.1175/JPO-D-13-024.1.

Buijsman, M. C., B. K. Arbic, J. A. M. Green, R. W. Helber, J. G. Richman, J. F. Shriver, P. G. Timko, and A. J. Wallcraft (2015), Optimizing internal wave drag in a forward barotropic model with semidiurnal tides, *Ocean Modelling*, *85*, 42–55.

Buijsman, M. C., J. K. Ansong, B. K. Arbic, J. G. Richman, J. F. Shriver, P. G. Timko, A. J. Wallcraft, C. B. Whalen, and Z. Zhao (2016), Impact of internal wave drag on the semidiurnal energy balance in a global ocean circulation model, *Journal of Physical Oceanography*, *46*, 1399–1419, doi:10.1175/JPO-D-15-0074.1.

Carter, G. S., O. B. Fringer, and E. D. Zaron (2012), Regional models of internal tides, *Oceanography*, *25(2)*, 56–65.

Chassignet, E. P., H. E. Hurlburt, E. J. Metzger, O. M. Smedstad, J. A. Cummings, G. R. Halliwell, R. Bleck, R. Baraille, A. J. Wallcraft, C. Lozano, H. L. Tolman, A. Srinivasan, S. Hankin, P. Cornillon, R. Weisberg, A. Barth, R. He, F. Werner, and J. Wilkin (2009), Global ocean prediction with the HYbrid Coordinate Ocean Model (HYCOM), *Oceanography*, *22*, 64–76.

Cummins, P. E., and L. Y. Oey (1997), Simulation of barotropic and baroclinic tides off Northern British Columbia, *Journal of Physical Oceanography*, *27*, 762–781.

Dushaw, B. D., P. F. Worcester, B. D. Cormuelle, B. M. Howe, and D. S. Luther (1995), Baroclinic and barotropic tides in the central North-Pacific Ocean determined from long-range reciprocal acoustic transmissions, *Journal of Physical Oceanography*, *25*, 631–647.

Egbert, G. D., and R. D. Ray (2003), Semi-diurnal and diurnal tidal dissipation from TOPEX/Poseidon altimetry, *Geophysical Research Letters*, *30 (17)*, doi: 10.1029/2003GL017676.

Egbert, G. G., and S. Y. Erofeeva (2002), Efficient inverse modeling of barotropic ocean tides, *Journal of Atmospheric and Oceanic Technology*, *19*, 183–204.

Egbert, G. G., and R. D. Ray (2000), Significant dissipation of tidal energy in the deep ocean inferred from satellite altimeter data, *Nature*, *405*, 775–778.

Egbert, G. G., and R. D. Ray (2001), Estimates of M_2 tidal energy dissipation from TOPEX/POSEIDON altimeter data, *Journal of Geophysical Research*, *106*, 22,475–22,502.

Emery, W. J., and R. E. Thomson (1997), *Data Analysis Methods in Physical Oceanography*, Pergamon.

Flierl, G. R. (1978), Models of vertical structure and the calibration of two-layer models, *Dynamics of Atmospheres and Oceans*, *2*, 341–381.

Gill, A. E. (1982), *Atmosphere-Ocean Dynamics*, Academic Press, New York.

Halliwell, G. R. (2004), Evaluation of vertical coordinate and vertical mixing algorithms in the HYbrid-Coordinate Ocean Model (HYCOM), *Ocean Modelling*, *7*, 285–322.

Hecht, M. W., and H. Hasumi (Eds.) (2008), *Ocean Modeling in an Eddying Regime*, Geophysical Monograph 117, American Geophysical Union, Washington, DC, 409 pp, http://dx.doi.org/10.1029/GM177.

Hendershott, M. C. (1972), The effects of solid earth deformation on global ocean tides., *Geophysical Journal of the Royal Astronomical Society*, *29*, 389–402.

Hibiya, T., M. Nagasawa, and Y. Niwa (2006), Global mapping of diapycnal diffusivity in the deep ocean based on the results of expendable current profiler (XCP) surveys, *Geophysical Research Letters*, *33*, L03,611, doi:10.1029/2005GL025218.

Hogan, T. F., M. Liu, J. A. Ridout, M. S. Peng, T. R. Whitcomb, B. C. Ruston, C. A. Reynolds, S. D. Eckermann, J. R. Moskaitis, N. L. Baker, J. P. McCormack, K. C. Viner, J. G. McLay, M. K. Flatau, L. Xu, C. Chen, and S. W. Chang (2014), The Navy Global Environmental Model, *Oceanography*, *27(3)*, 116–125.

Jayne, S. R., and L. C. St Laurent (2001), Parameterizing tidal dissipation over rough topography, *Geophysical Research Letters*, *28*, 811–814.

Kerry, C., B. Powell, and G. Carter (2014), The impact of subtidal circulation on internal-tide-induced mixing in the Philippine sea, *Journal of Physical Oceanography*, *44*, 3209–3224, doi:10.1175/JPO-D-13-0142.1.

Kerry, C., B. Powell, and G. Carter (2016), Quantifying the incoherent M_2 internal tide in the Philippine Sea, *Journal of Physical Oceanography*, *46*, 2483–2491, doi:10.1175/JPO-D-16-0023.1.

Kunze, E., L. Rosenfield, G. Carter, and M. C. Gregg (2002), Internal waves in Monterey Submarine Canyon, *Journal of Physical Oceanography*, *32*, 1890–1913.

Lighthill, M. J. (1969), Dynamic response of the Indian Ocean to the onset of the southwest monsoon, *Philosophical Transactions of the Royal Society of London. Series A*, *265 (1159)*, 45–92.

Merrifield, M. A., and P. E. Holloway (2002), Model estimates of M_2 internal tide energetics at the Hawaiian Ridge, *Journal of Geophysical Research*, *107, 3179*, doi: 10.1029/2001JC000996.

Merrifield, M. A., P. E. Holloway, and T. M. S. Johnston (2001), The generation of internal tides at the Hawaiian Ridge, *Geophysical Research Letters*, *28*, 559–562.

Metzger, E. J., O. M. Smedstad, P. G. Thoppil, H. E. Hurlburt, J. A. Cummings, A. J. Wallcraft, L. Zamudio, D. S. Franklin, P. G. Posey, M. W. Phelps, P. J. Hogan, F. L. Bub, and C. J. DeHaan (2014), US Navy operational global ocean and arctic ice predcition system, *Oceanography*, *27 (3)*, 32–43.

Mitchum, G. T., and S. M. Chiswell (2000), Coherence of internal tide modulations along the hawaiian ridge, *Journal of Geophysical Research*, *105 (C12)*, 28,653–28,661.

Müller, M. (2013), On the space- and time-dependence of barotropic-to-baroclinic tidal energy conversion, *Ocean Modelling*, *72*, 242–252, doi:10.1016/j.ocemod.2013.09.00.

Müller, M., J. Y. Cherniawsky, M. G. G. Foreman, and J. S. Storch von (2012), Global M_2 internal tide and its seasonal variability from high resolution ocean circulation and tide modeling, *Geophysical Research Letters*, *39, L19607*, doi:10.1029/2012GL053320.

Müller, M., J. Cherniawsky, M. Foreman, and J. S. von Storch (2014), Seasonal variation of the M_2 tide, *Ocean Dynamics*, *64(2)*, 159–177, doi:10.1007/s10236-013-0679-0.

Müller, M., B. K. Arbic, J. G. Richman, J. F. Shriver, E. L. Kunze, R. B. Scott, A. J. Wallcraft, and L. Zamudio (2015), Toward an internal gravity wave spectrum in global ocean models, *Geophysical Research Letters*, *42*, 3474–3481, doi:10.1002/2015GL063365.

Munk, W., and C. Wunsch (1998), Abyssal recipes ii: energetics of tidal and wind mixing, *Deep-Sea Research I*, *45*, 1977–2010.

Nash, J. D., M. H. Alford, and E. Kunze (2005), Estimating internal wave energy fluxes in the ocean, *Journal of Atmospheric and Oceanic Technology*, *22*, 1551–1570.

Ngodock, H. E., I. Souopgui, A. J. Wallcraft, J. G. Richman, J. F. Shriver, and B. K. Arbic (2016), On improving the accuracy of the M_2 barotropic tides embedded in a high-resolution global ocean circulation model, *Ocean Modelling*, *97*, 16–26, doi:

10.1016/j.ocemod.2015.10.011.

Niwa, Y., and T. Hibiya (2011), Estimation of baroclinic tide energy available for deep ocean mixing based on three-dimensional global numerical simulations, *Journal of Oceanography*, *67*, 493–502.

Ponte, A. L., and P. Klein (2015), Incoherent signature of internal tides on sea level in idealized numerical simulations, *Geophysical Research Letters*, *42*, 1520–1526, doi: 10.1002/2014GL062583.

Rainville, L., T. M. Shaun Johnston, G. S. Carter, M. A. Merrifield, R. Pinkel, P. F. Worcester, and B. D. Dushaw (2010), Interference pattern and propagation of the m_2 internal tide south of the Hawaiian Ridge, *Journal of Physical Oceanography*, *40*, 311–325.

Ray, R. D. (1998), Ocean self-attraction and loading in mumerical tidal models, *Marine Geodesy*, *21*, 181–192.

Ray, R. D., and G. T. Mitchum (1996), Surface manifestation of internal tides generated near Hawaii, *Geophysical Research Letters*, *23*, 2101–2104.

Ray, R. D., and G. T. Mitchum (1997), Surface manifestation of internal tides in the deep ocean: Observations from altimetry and tide gauges, *Progress in Oceanography*, *40*, 135–162.

Ray, R. D., and E. D. Zaron (2011), Non-stationary internal tides observed with satellite altimetry, *Geophysical Research Letters*, *38, L17609*, doi:10.1029/2011GL048617.

Ray, R. D., and E. D. Zaron (2016), M_2 internal tides and their observed wavenumber spectra from satellite altimetry, *Journal of physical oceanography*, *46*, 3–22, doi: 10.1175/JPO-D-15-0065.1.

Richman, J. G., B. K. Arbic, J. F. Shriver, E. J. Metzger, and A. J. Wallcraft (2012), Inferring dynamics from the wavenumber spectra of an eddying global ocean model with embedded tides, *Journal of Geophysical Research*, *117, C12012*, doi: 10.1029/2012JC008364.

Rocha, C. B., T. K. Chereskin, S. T. Gille, and D. Menemenlis (2016), Mesoscale to submesoscale wavenumber spectra in Drake Passage, *Journal of Physical Oceanogarphy*, *46*, doi:10.1175/JPO-D-15-0087.1.

Shriver, J. F., B. K. Arbic, J. G. Richman, R. D. Ray, E. J. Metzger, A. J. Wallcraft, and P. G. Timko (2012), An evaluation of the barotropic and internal tides in a high resolution global ocean circulation model, *Journal of Geophysical Research*, *117, C10024*, doi:10.1029/2012JC008170.

Shriver, J. F., J. G. Richman, and B. K. Arbic (2014), How stationary are the internal tides in a high resolution global ocean circulation model?, *Journal of Geophysical Research*, *119*, doi:10.1002/2013JC009423.

Simmons, H. L. (2008), Spectral modification and geographic redistribution of the semi-diurnal internal tide, *Ocean Modelling*, *21*, 126–138.

Simmons, H. L., and M. H. Alford (2012), Simulating the long-range swell of internal waves generated by ocean storms, *Oceanography*, *25 (2)*, 30–41.

Simmons, H. L., R. W. Hallberg, and B. K. Arbic (2004), Internal wave generation in a global baroclinic tide model, *Deep-Sea Research II*, *51*, 3043–3068.

St. Laurent, L., and C. Garrett (2002), The role of internal tides in mixing the deep ocean, *Journal of Physical Oceanography*, *32*, 2882–2899.

Stammer, D., R. D. Ray, O. B. Andersen, B. K. Arbic, W. Bosch, L. Carrere, Y. Cheng, D. S. Chinn, B. D. Dushaw, G. D. Egbert, S. Y. Erofeeva, H. S. Fok, J. A. M. Green, S. Griffiths, M. A. King, V. Lapin, F. G. Lemoine, S. Luthcke, F. Lyard, J. Morison, M. Mller, L. Padman, J. G. Richman, J. F. Shriver, C. K. Shum, E. Taguchi, and Y. Yi (2014), Accuracy assessment of global barotropic ocean tide models, *Reviews of Geophysics*, *52*, doi:10.1002/2014RG000450.

Thoppil, P. G., J. G. Richman, and P. J. Hogan (2011), Energetics of a global ocean circulation model compared to observations, *Geophysical Research Letters*, *38, L15607*, doi:10.1029/2011GL048347.

Timko, P. G., B. K. Arbic, J. G. Richman, R. B. Scott, E. J. Metzger, and A. J. Wallcraft (2012), Skill tests of three-dimensional tidal currents in a global ocean model: A look at the North Atlantic, *Journal of Geophysical Research*, *117, C08014*, doi: 10.1029/2011JC007617.

Timko, P. G., B. K. Arbic, J. G. Richman, R. B. Scott, E. J. Metzger, and A. J. Wallcraft (2013), Skill testing a three-dimensional global tide model to historical current meter records, *Journal of Geophysical Research*, *118*, 6914–6933, doi:10.1002/2013JC009071.

Wunsch, C. (1975), Internal tides in the ocean, *Rev. Geophys. Space Phys.*, *13*, 167–182.

Wunsch, C., and R. Ferrari (2004), Vertical mixing, energy and the general circulation of the ocean., *Annual Review of Fluid Mechanics*, *36*, 281–314.

Wunsch, C., and D. Stammer (1997), Atmospheric loading and the oceanic "inverted barometer" effect, *Reviews of geophysics*, *35*, 79–107.

Zaron, E. D. (2015), Nonstationary internal tides observed using dual-satellite altimetry, *Journal of Physical Oceanography*, *45*, 2239–2246, doi:10.1175/JPO-D-15-0020.1.

Zaron, E. D., and G. D. Egbert (2014), Time-variable refraction of the internal tide at the Hawaiian Ridge, *Journal of Physical Oceanography*, *44*, 538–557, doi:10.1175/JPO-D-12-0238.1.

Zhao, Z., M. H. Alford, J. A. MacKinnon, and R. Pinkel (2010), Long-range propagation of the semi-diurnal internal tide from the Hawaiian ridge, *Journal of Physical Oceanography*, *40*, 713–736.

Zhao, Z., M. H. Alford, J. B. Girton, L. Rainville, and H. L. Simmons (2016), Global observations of open-ocean mode 1 M_2 internal tides, *Journal of Physical Oceanography*, *46*, 1657–1684, doi:10.1175/JPO-D-15-0105.1.

Figure 1. Locations of 79 historical moorings. The rectangles denote regions identified by *Shriver et al.* [2012] as hotspot regions of internal tides in HYCOM.

Figure 2. (*a*) Magnitude (kW/m) of vertically-integrated semidiurnal baroclinic energy fluxes from one month of 1/12.5° HYCOM output. The rectangles denote regions identified by *Shriver et al.* [2012] as hotspot regions in HYCOM. (*b*) Semidiurnal internal tide conversion (background color; in $\mathrm{mW/m^2}$) and energy flux vectors from one month of 1/12.5° HYCOM (black arrows, plotted at every 768*th* grid point for clarity). Fluxes with $|\mathbf{F}| < 0.8\,\mathrm{kW/m}$ are not plotted and reference arrows are plotted in the upper left corner over Asia.

Figure 3. The total (potential plus kinetic) baroclinic energy density in the first two vertical modes (left axes) and the fraction of energy in mode-2 (right axes; triangle markers) at each mooring location for the 1/25° HYCOM simulations. The locations are ordered by decreasing amounts of total (mode-1 plus mode-2) baroclinic energy density.

Figure 4. The RMS of low-frequency eddy kinetic energy (EKE) in (a) 1/12.5° and (b) 1/25° HYCOM simulations versus observations, computed from 2-day low-pass horizontal velocity fields.

Figure 5. Example time series of 1/25° HYCOM semidiurnal mode-1 baroclinic energy flux (a) magnitude and (b) direction, at a location north of Hawai'i (latitude 40.6° North, longitude 197.0° East). The fluxes are divided into 50 % overlapping 30−day windows. The vertical bars are envelopes of the magnitude-only (in (a)) and direction-only (in (b)) variabilities computed over all locations (see equations 13-15).

Figure 6. As in Figure 5 but for the mooring location with latitude 35.55° North and longitude 142.66° East.

Figure 7. (a,b): The RMS variability (RMS) and mean magnitude of semidiurnal mode-1 energy fluxes, in (a) 1/25° HYCOM and (b) observations. (c,d): The normalized RMS variability (NRMS) in (c) HYCOM and (d) observations. The values are plotted in descending order according to the mean magnitude of the energy fluxes for each dataset.

Figure 8. As in Figure 7 but for the mode-2 fluxes.

Figure 9. [Left-Panels] Log-log scatter plot of semidiurnal mode 1 energy flux magnitudes in (a) 1/25° HYCOM versus *Alford and Zhao* [2007] observations, (c) full-column versus subsampled HYCOM output. (e) The angle between the observed and modeled flux vectors at each location (left axis) and the time-averaged flux magnitude (right axis). The locations in (e) are ordered in decreasing order of the HYCOM time-averaged flux magnitude. [Right-Panels] Same as in left panels but for the mode-2 fluxes.

Figure 10. Global map of depth-integrated semidiurnal energy fluxes computed for the (a) mode-1 and (b) mode-2 waves in 1/25° HYCOM. Red and blue arrows denote modeled and observed fluxes respectively. Arrow lengths are logarithmic with reference arrows shown at upper left over Asia. The rectangles denote regions identified by *Shriver et al.* [2012] as hotspot regions in HYCOM.

Figure 11. [Top-Panels] Map of depth-integrated semidiurnal energy fluxes computed for the (a) mode-1 and (b) mode-2 cases in 1/25° HYCOM (red arrows) and observations (blue arrows) from the IWAP experiment [*Zhao et al.*, 2010]. Arrow lengths are logarithmic and reference arrows are shown at the upper left corner of each plot. [Bottom-Panels] (c) The angle between the observed and HYCOM mode-1 flux vectors in (a) (left axes) and the mean flux magnitude (right axis). (d) As in (c) but for mode-2.

Figure 12. Comparison of 1/12.5° HYCOM total semidiurnal baroclinic energy fluxes computed via the z-level and isopycnal methods. (a) The magnitude of the mean fluxes, (b) the direction of the mean fluxes (measured counter-clockwise from due East), and (c) the angle between the mean fluxes derived from both methods at each location. The locations in (c) are ordered by decreasing kinetic energy density levels, and the dashed black lines in (a) − (b) are one-to-one lines.

Table 1. RMS variability (RMS; in kW/m) and Normalized RMS variability (NRMS) of semidiurnal energy fluxes from 1/25° HYCOM and observations (see equations 13-15). Results are shown for modes 1 and 2, and for both full-column and vertically subsampled (in brackets) output. Furthermore, the magnitude-only, magnitude-weighted direction, direction-only, and total avariabilities are given.

Mode 1				
	RMS		NRMS	
	HYCOM	Observations	HYCOM	Observations
Magnitude-only	0.194(0.290)	0.364	0.861(1.240)	1.327
Magnitude-weighted direction	0.146(0.206)	0.343	0.658(0.846)	1.103
direction-only	0.158(0.218)	0.327	0.635(0.719)	0.919
Total	0.246(0.361)	0.503	1.096(1.518)	1.738

Mode 2				
	RMS		NRMS	
	HYCOM	Observations	HYCOM	Observations
Magnitude-only	0.057(0.088)	0.139	2.218(1.955)	2.544
Magnitude-weighted direction	0.042(0.067)	0.103	1.345(1.369)	1.597
direction-only	0.047(0.058)	0.083	0.965(1.004)	1.057
Total	0.071(0.111)	0.175	2.635(2.411)	3.037

Table 2. Statistical measures of the comparison between semidiurnal baroclinic energy fluxes from 1/25° HYCOM and observations. Regression coefficient A; Correlation coefficient R; Ratio of global mean of model to observed magnitude of flux γ (see equations 16-18 and associated text). γ_{dir} is the fraction of locations at which the angle between the observed and modeled flux vectors $\phi_b \leq 60°$. Results are shown for both mode 1 and mode 2, and for both full-column and vertically subsampled data (see text for explanation).

	Mode 1		Mode 2	
	Full-column	Subsampled	Full-column	Subsampled
A	0.68	0.82	0.58	0.55
R	0.88	0.88	0.49	0.42
R^2	0.77	0.77	0.24	0.18
γ	0.80	0.96	0.60	0.68
γ_{dir}	0.70	0.73	0.38	0.44

Table 3. Semidiurnal internal tide energy flux magnitude (in kW/m) and direction (counterclockwise from east; in degrees) from 1/25° HYCOM and observations at 3 HYCOM hotspot locations. Results are shown for both mode 1 and mode 2, and calculations from subsampled HYCOM are in brackets.

Mode 1					
Location		Flux Magnitude		Flux Direction	
Lat	Lon	Observation	HYCOM	Observation	HYCOM
28.01°N	207.92°E	1.08	0.81(0.75)	15.46°	5.06°(7.58°)
28.08°N	207.92°E	0.14	0.99(0.70)	90.35°	81.75°(93.20°)
28.01°N	151.92°E	1.41	1.49(1.05)	22.06°	37.07°(48.52°)

Mode 2					
Location		Flux Magnitude		Flux Direction	
Lat	Lon	Observation	HYCOM	Observation	HYCOM
28.01°N	207.92°E	0.27	0.14(0.08)	28.13 °	6.12°(28.07°)
28.08°N	207.92°E	0.04	0.17(0.17)	283.84°	119.42°(61.14°)
28.01°N	151.92°E	0.32	0.05(0.04)	104.15°	122.64°(148.76°)

Table 4. Semidiurnal internal tide energy flux magnitude (in kW/m) and direction (counterclockwise from east; in degrees) from 1/25° HYCOM and IWAP observational data [*Zhao et al.*, 2010]. Results are shown for both mode 1 and mode 2 (in brackets).

Mooring	Location		Flux Magnitude		Flux Direction (°)	
name	Lat	Lon	Observation	HYCOM	Observation	HYCOM
MP1	25.5°N	194.9°E	3.48(0.12)	6.28(0.11)	62.0(40.3)	47.3(339.7)
MP2	27.8°N	196.0°E	1.08(0.11)	2.98(0.14)	46.4(4.0)	50.8(21.9)
MP3	28.9°N	196.5°E	1.65(0.04)	2.51(0.04)	47.2(123.8)	97.7(150.1)
MP4	30.1°N	197.1°E	3.14(1.50)	2.12(0.06)	31.2(38.3)	57.5(36.9)
MP5	32.9°N	198.6°E	0.92(0.88)	3.43(0.05)	54.1(82.9)	65.2(4.0)
MP6	37.1°N	200.8°E	1.26(0.23)	1.13(0.06)	78.7(23.3)	82.9(338.6)

Figure 1.

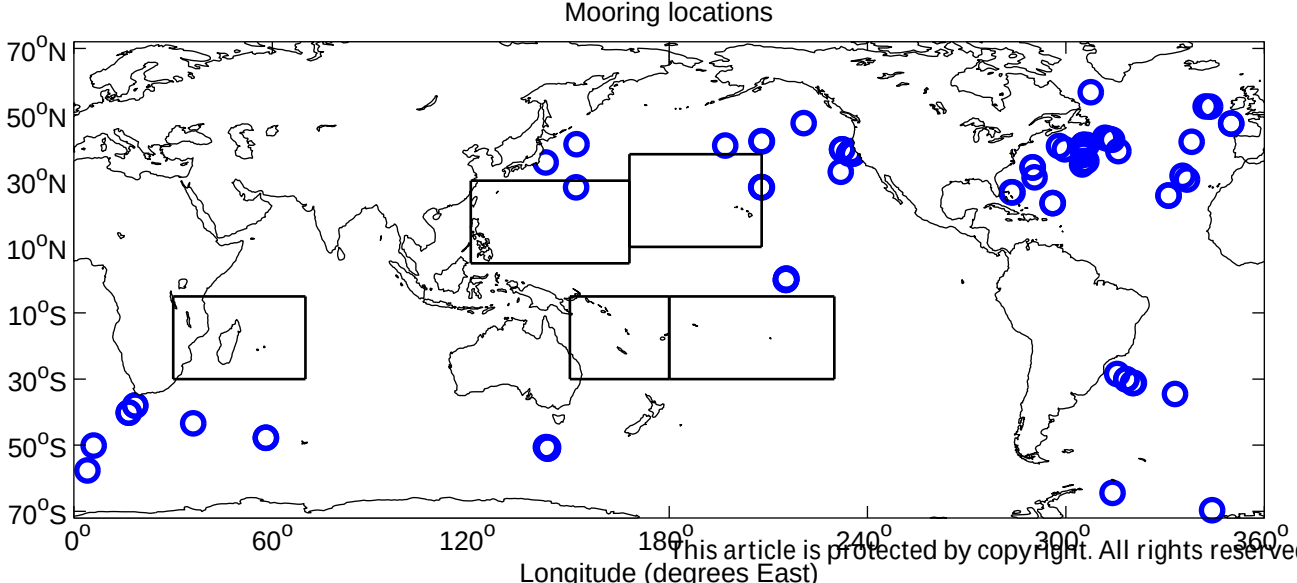

Figure 2.

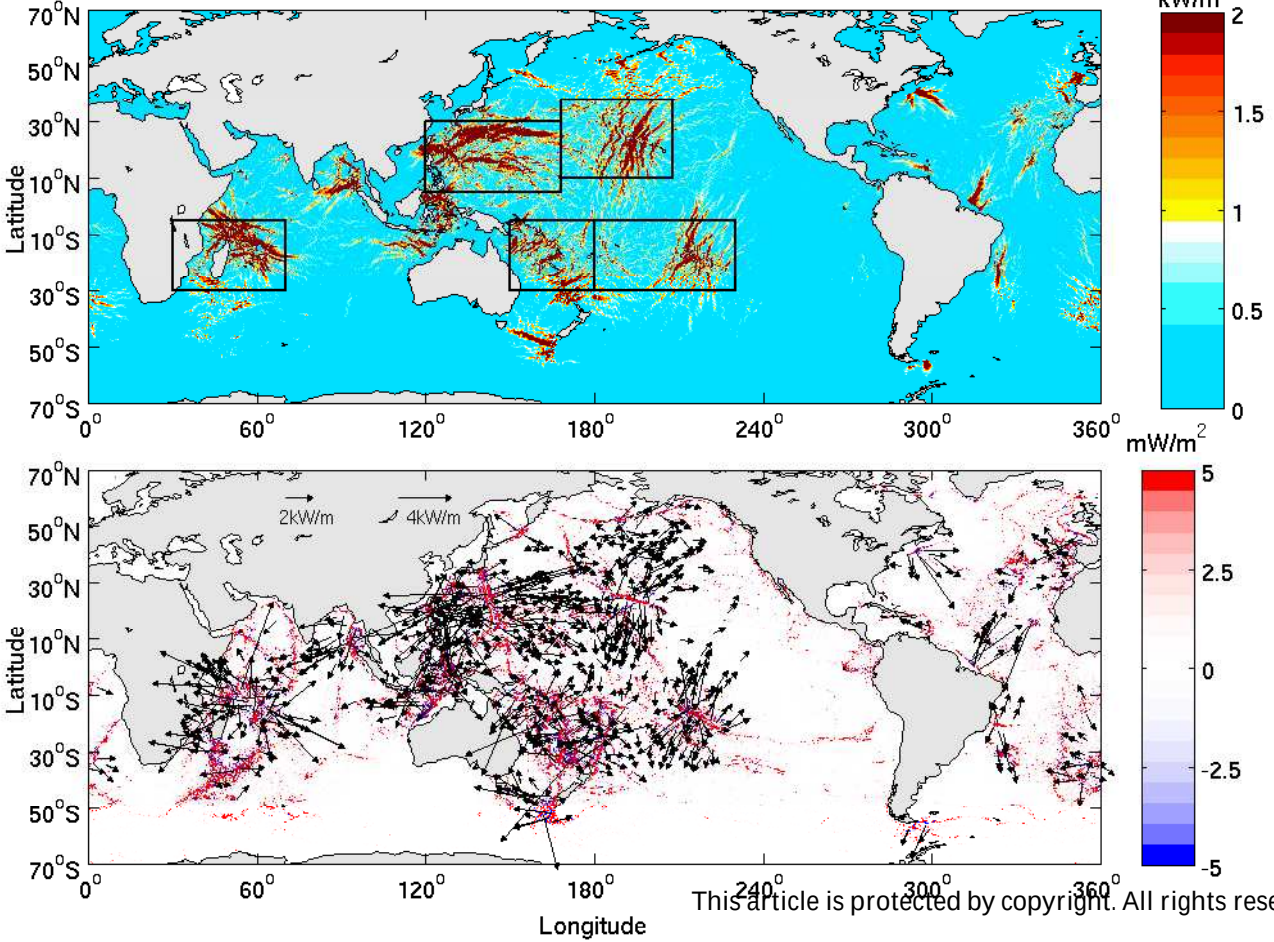

Figure 3.

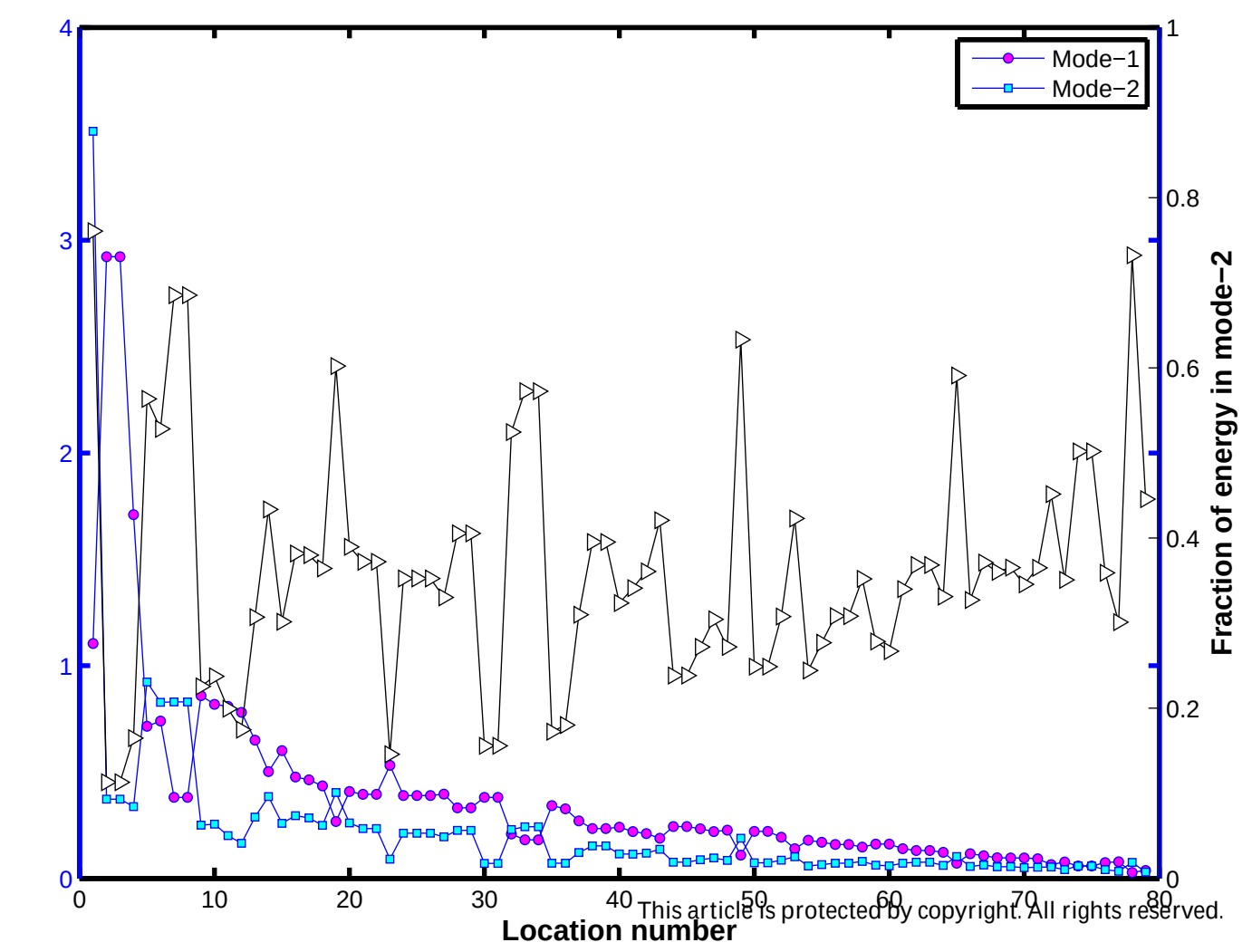

Figure 4.

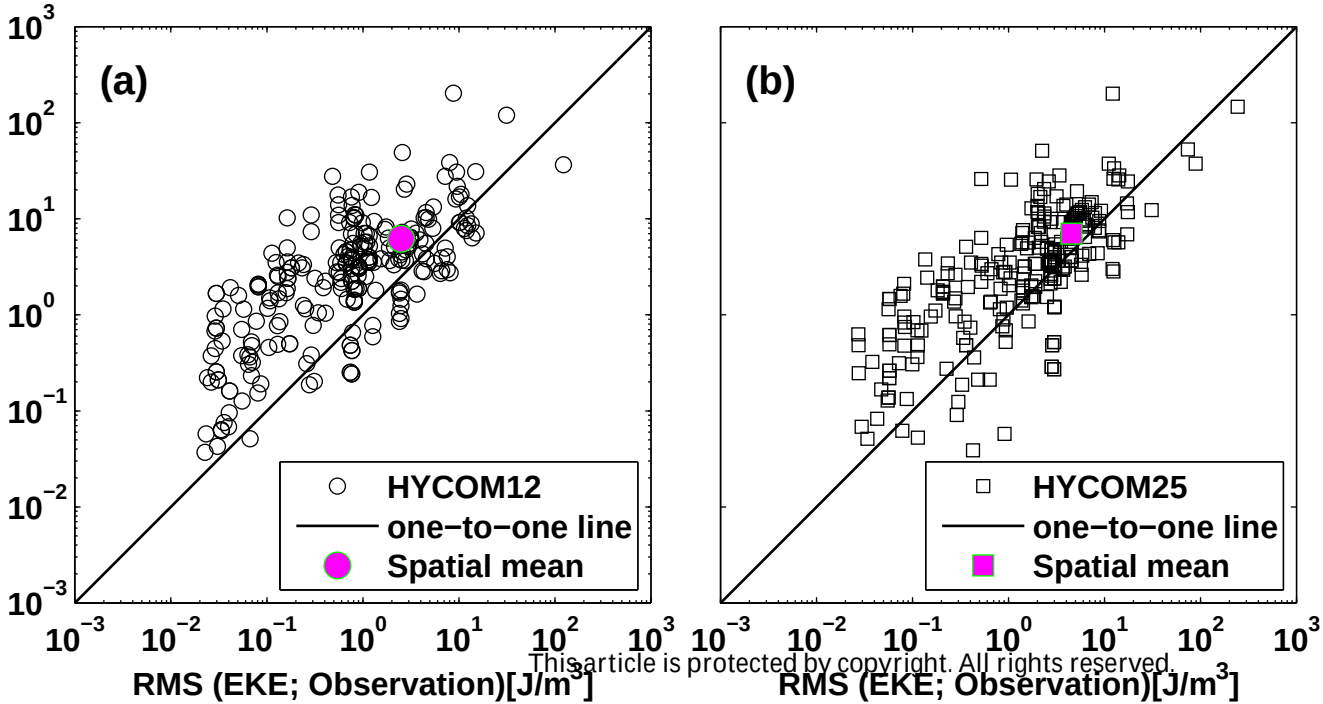

Figure 5.

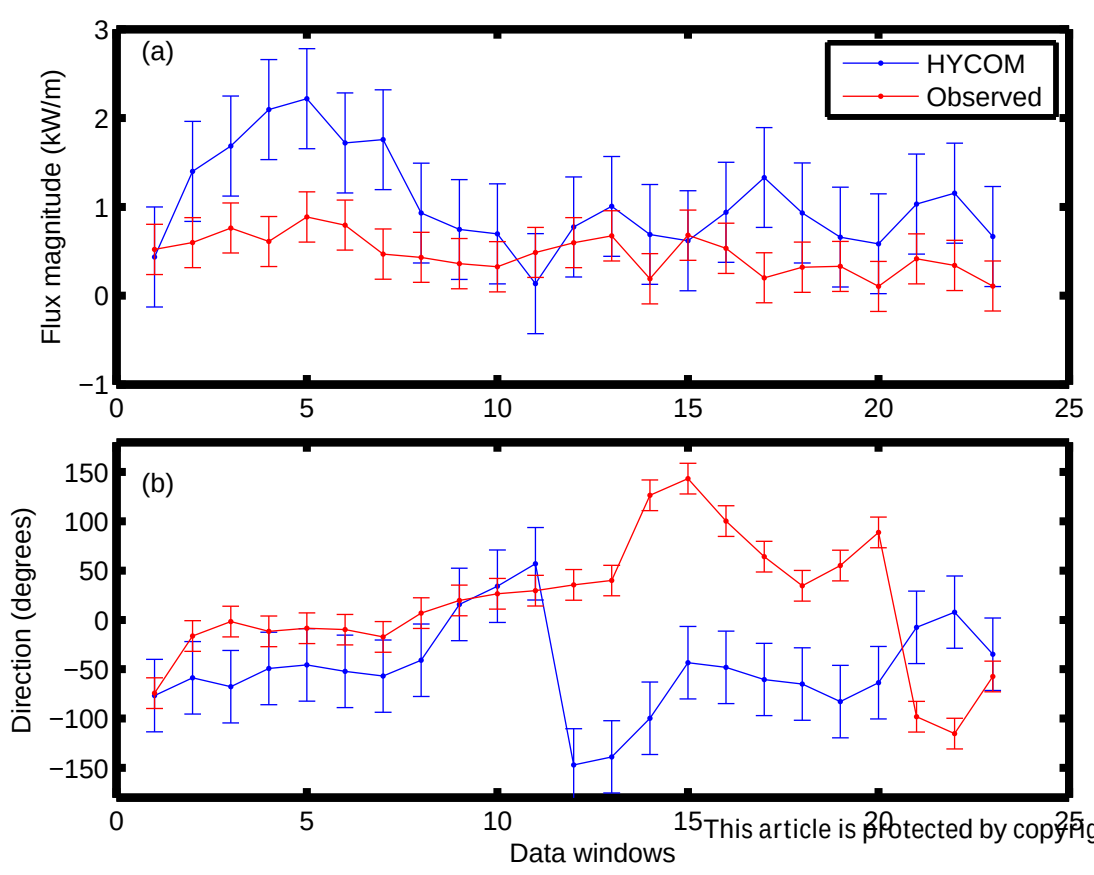

Figure 6.

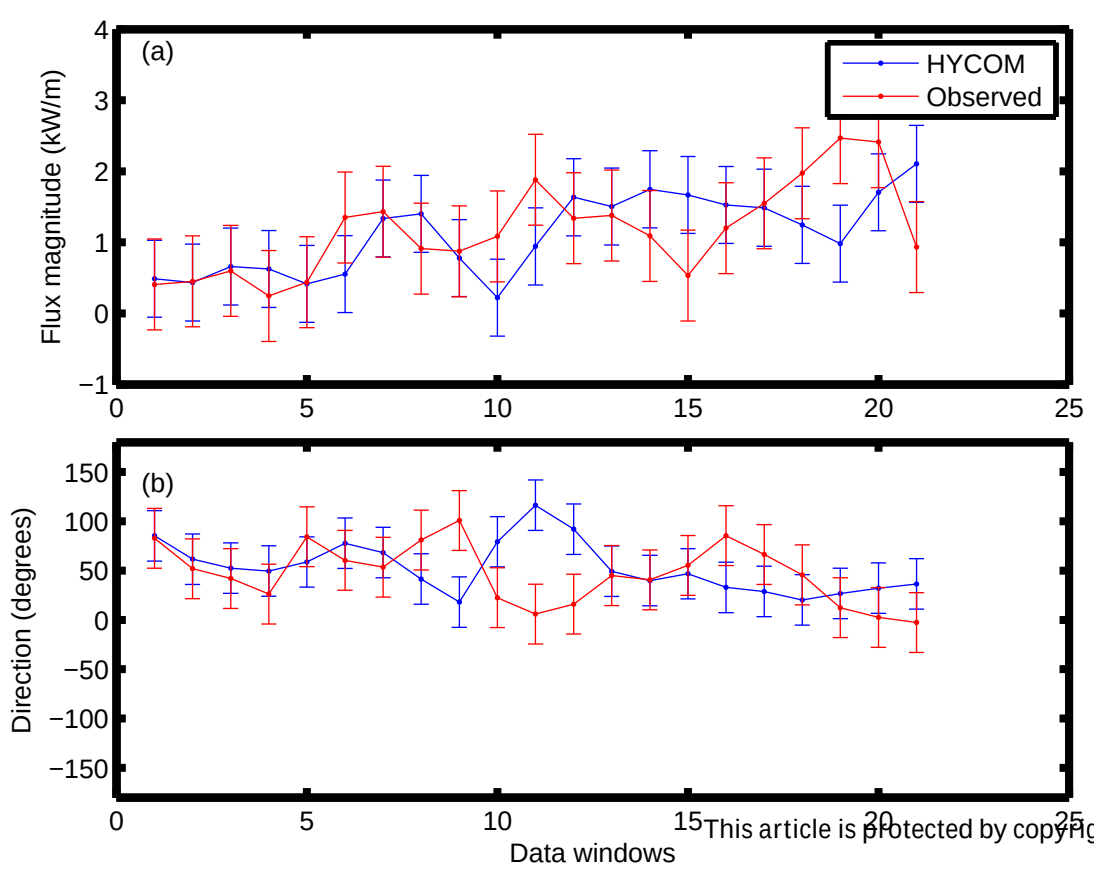

Figure 7.

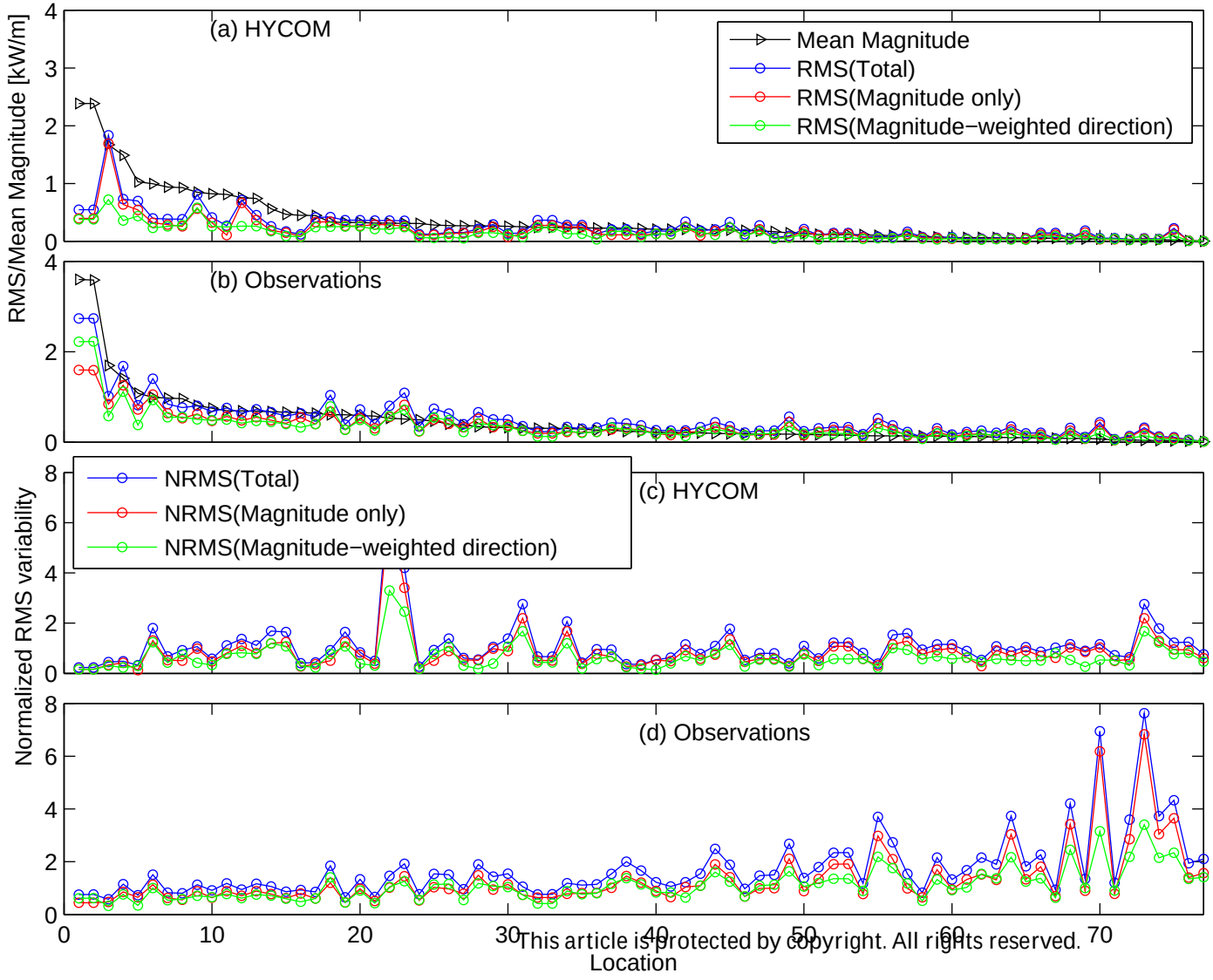

Figure 8.

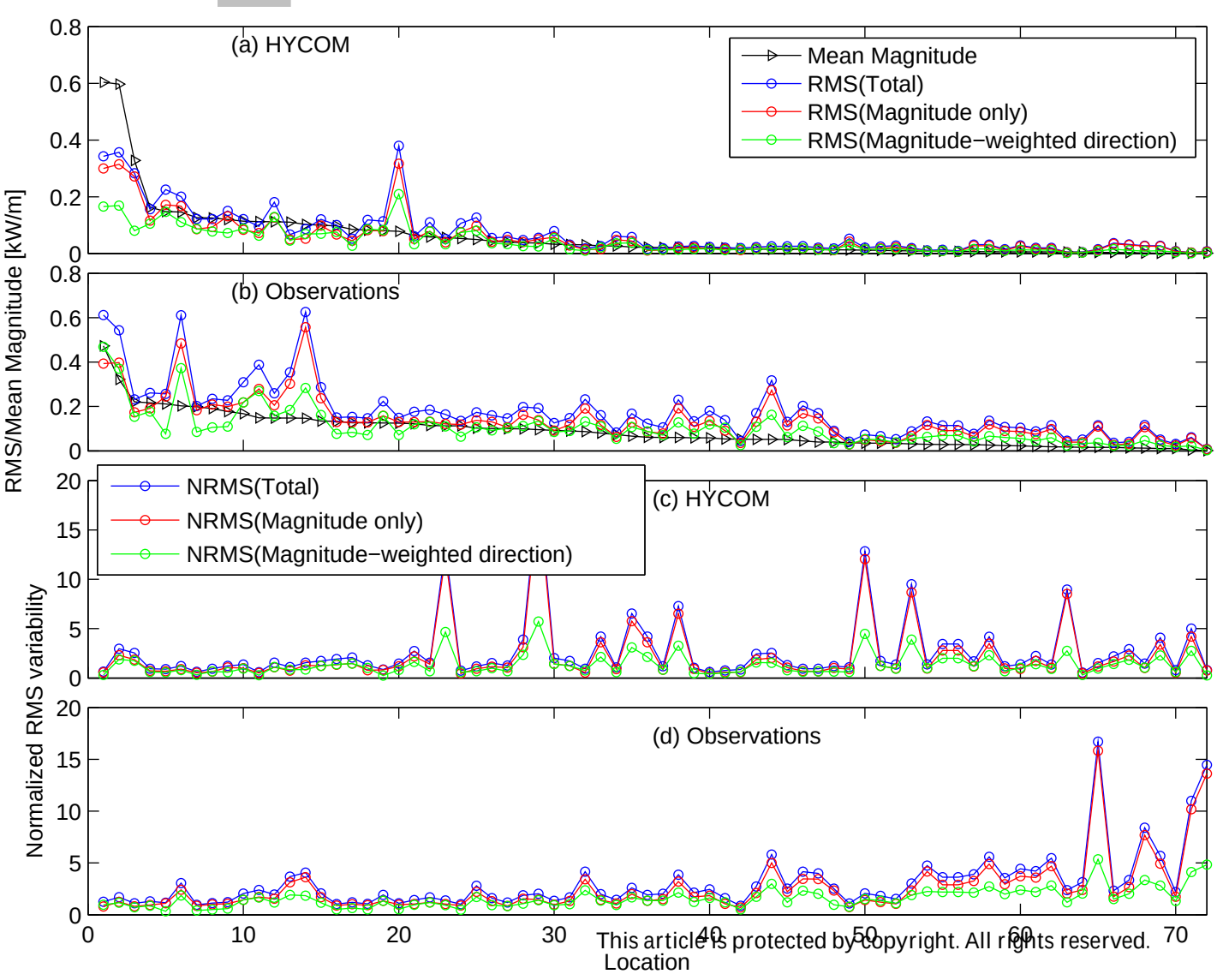

Figure 9.

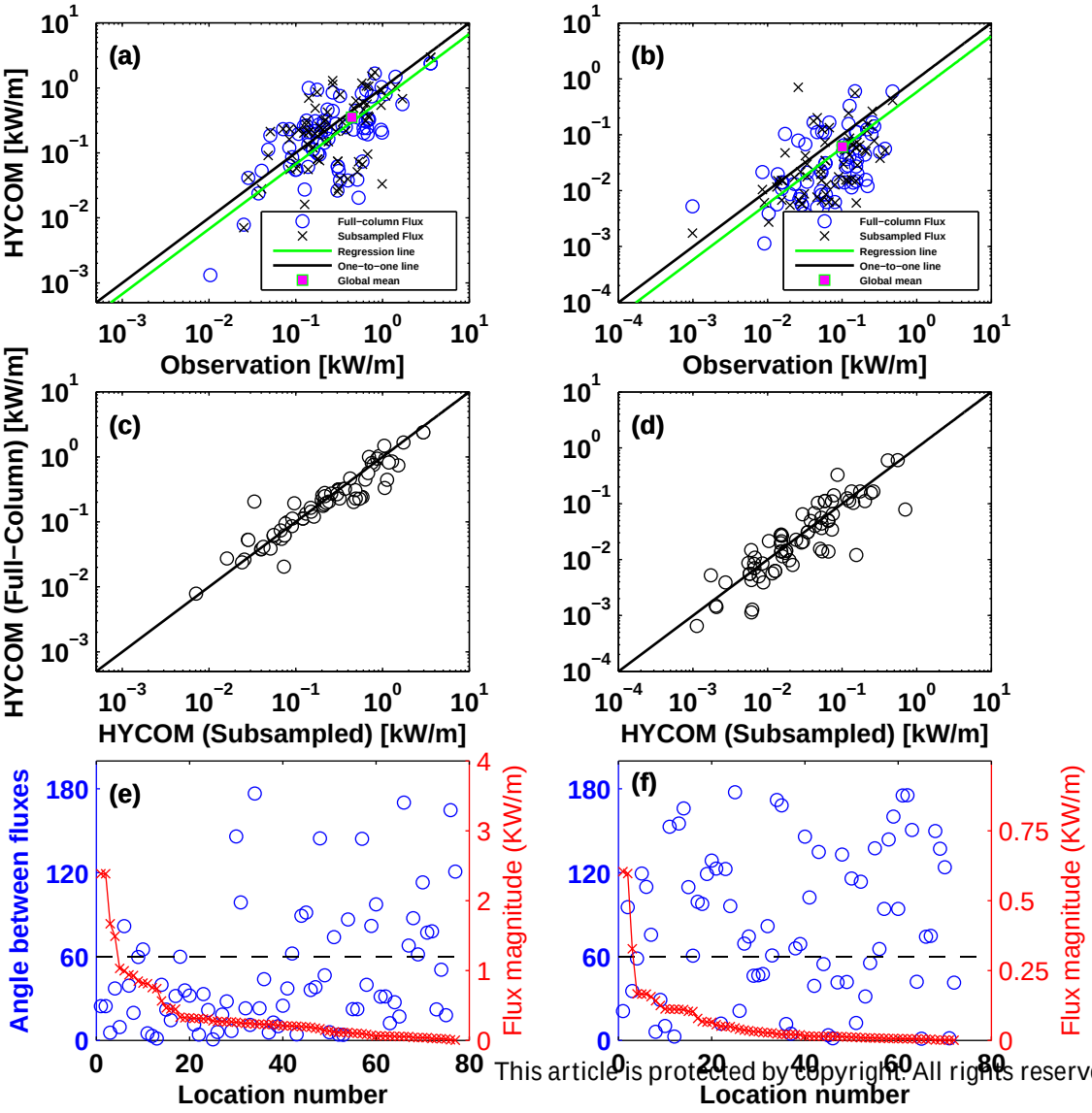

Figure 10.

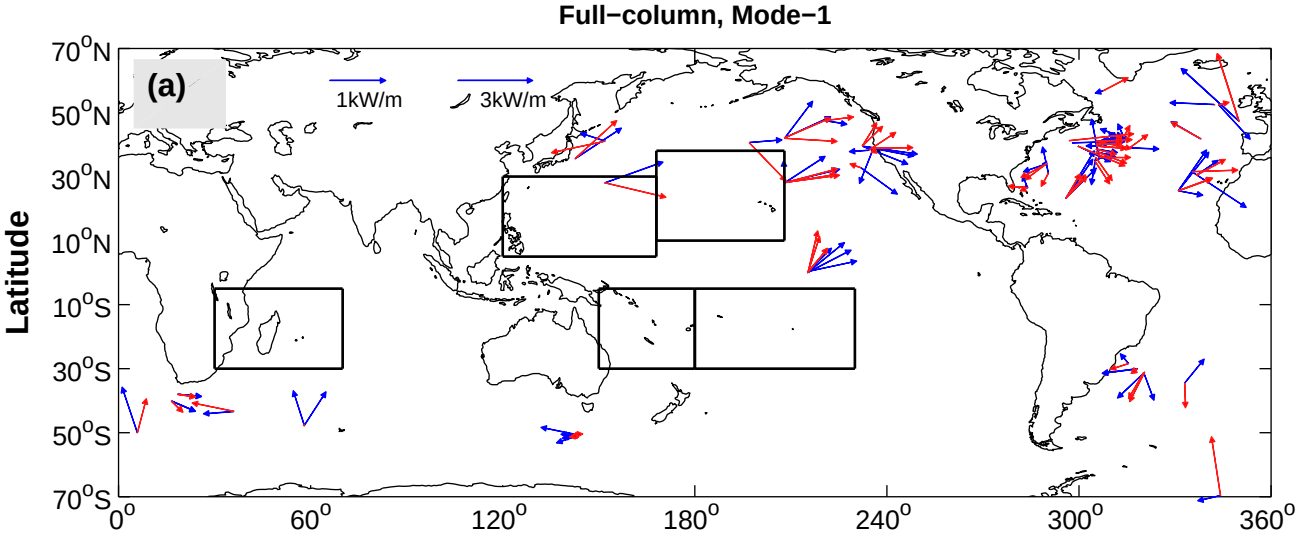

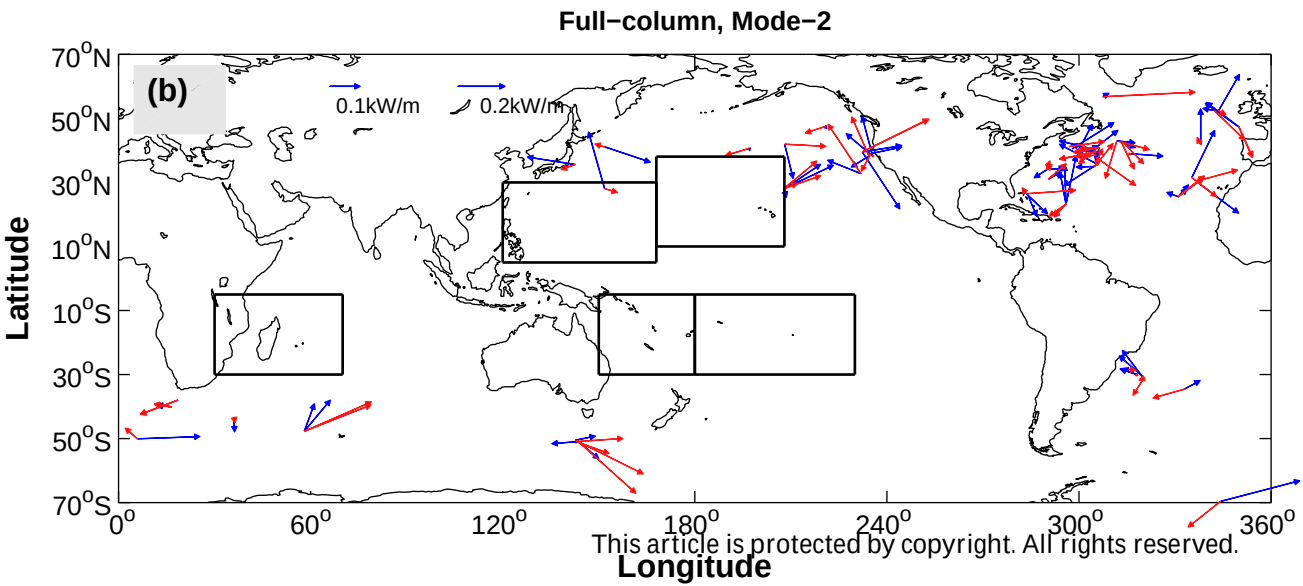

Figure 11.

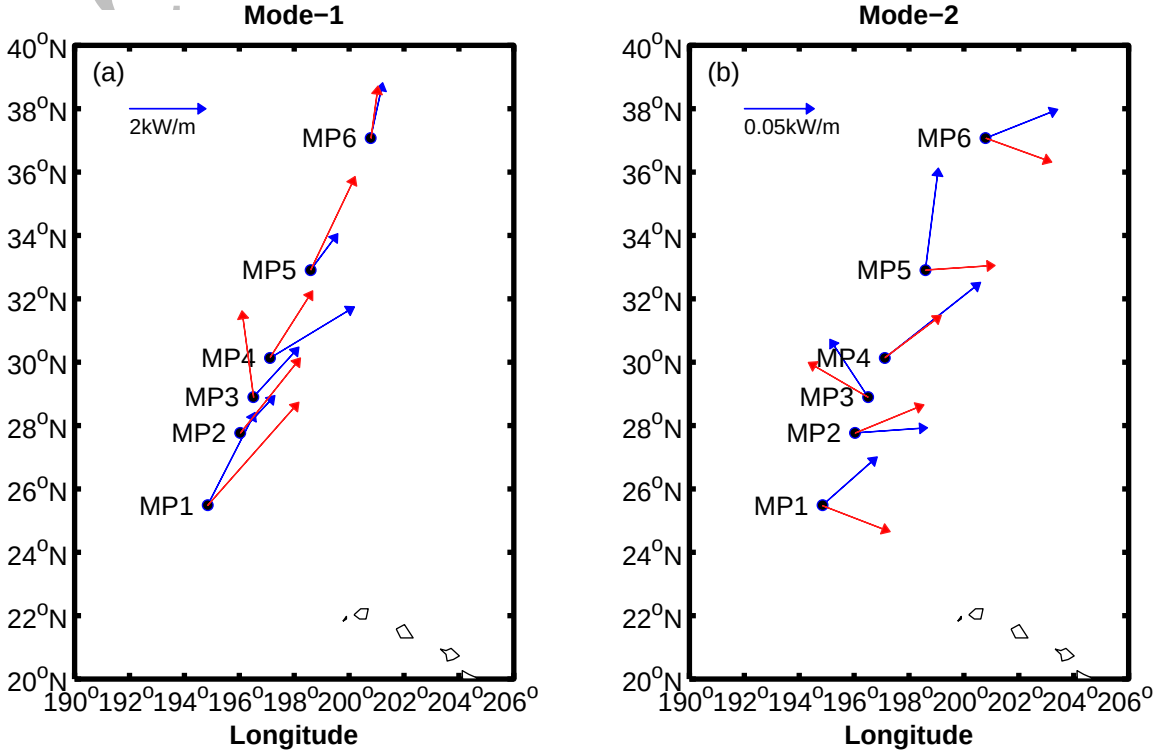

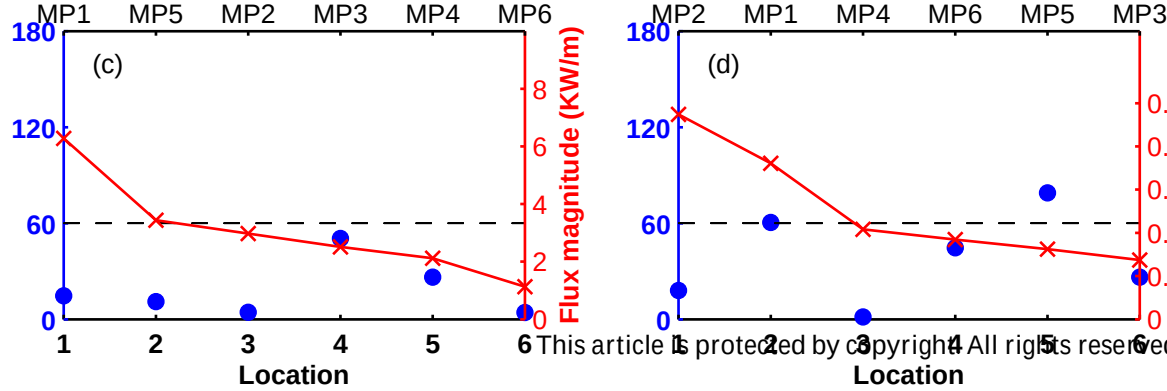

Figure 12.